Theories of strain analysis from shape fabrics: A perspective using hyperbolic geometry

Atsushi Yamaji*

Division of Earth and Planetary Sciences, Graduate School of Science, Kyoto University, Sakyo-ku, Kyoto 606-8502, Japan

ARTICLE INFO

ABSTRACT

A parameter space is proposed for unifying the theories of two-dimensional strain analysis, where strain markers are approximated by ellipses with a prescribed area. It is shown that the theories are unified by hyperbolic geometry, the oldest and simple non-Euclidean geometry. The hyperboloid model of the geometry is used for this purpose. Ellipses normalized by their areas are represented by points on the unit hyperboloid, the curved surface in a non-Euclidean space. Dissimilarity between ellipses is defined by the distance between the points that represent the ellipses. The merit of introducing the geometry comes from the fact that this distance equals the doubled natural strain needed to transform one ellipse to another. Thus, the introduction is natural and convenient for strain and error analyses. Equal-area and gnomonic projections of the hyperboloid are introduced for the R_f/ϕ and kinematic vorticity analyses, respectively. In our formulation, the strain ellipse optimal for a set of R_f/ϕ data is obtained as the centroid of the points corresponding to the data on the hyperboloid, and the dispersion of the points shows the uncertainty of the optimal strain. By means of a bootstrap method, the confidence region of the strain is drawn upon the surface, and equal-area projection from the surface to a Euclidean plane shows the dispersion of the points and the size of the confidence region. In addition, our formulation provides a new graphical technique for kinematic vorticity analysis using the gnomonic projection. The technique yields the optimal kinematic vorticity number with its uncertainty.

© 2008 Elsevier Ltd. All rights reserved.

1. Introduction

Strain analysis is an essential technique for complete understanding of the finite deformations of the lithosphere. Various methods have been developed to evaluate strain or deformation of rocks (e.g., Haughton, 1856; Cloos, 1947; Flinn, 1956; Wellman, 1962; Ramsay, 1967; Hossack, 1968; Ramsay and Huber, 1983; Passchier and Trouw, 2005). Their theories are based on continuum mechanics, but are formed ad hoc to deal with specific issues such as the determination of strain from R_f/ϕ data (Ramsay, 1967; Dunnet, 1969). The present paper aims at presenting a common basis for formulating the theories of two-dimensional strain analysis that use ellipses for approximating the shapes of strain markers in deformed rocks.

This work was triggered when I became aware of the equivalence of an equation of two-dimensional strain analysis by Dunnet (1969) with a formula of hyperbolic geometry, the non-Euclidean geometry found by Lobachevskiĭ, Bolyai and Gauss in the early 19th Century (Faber, 1983). This paper demonstrates that the geometry allows us not only to reformulate theories of two-dimensional strain analysis

but also to establish a basis for estimating the optimal strain and its error by means of formal statistical methodology.

This paper is organized as follows. Important quantities and symbols used in this paper are introduced in Section 2. Section 3 introduces the connection between two-dimensional deformation and hyperbolic geometry, which has alternative formulations. Among them, we adopt the formulation called the hyperboloid model (Section 4). The utility of the model for two-dimensional analysis is explained in Section 5. That is, the model provides the common basis for the theories of the analysis, and leads to new graphical methods. We take R_f/ϕ strain analysis, center-to-center strain analysis and kinematic vorticity analysis as examples. Two different plots, i.e., equal-area and gnomonic nets, for shape fabric are proposed in Section 4 and used in Section 5.

In this paper, it is assumed that all the grains in a rock suffered a homogeneous deformation or rotations by spatially steady flow. It is beyond the scope of this paper to deal with the cases to which the assumption does not apply.

2. Notation

Let us, first, define some important symbols for dealing with ellipses. As it is not easy to estimate volume changes accompanied

* Fax: +81 75 753 4189.
   E-mail address: yamaji@kueps.kyoto-u.ac.jp

by tectonic deformations from strain markers, the changes are ignored throughout of this paper. And, every ellipse is assumed to have an area of π, which is equal to that of a unit circle. As a result, we deal only with the aspect ratios and major-axis orientations of ellipses. The orientations are measured from a reference line that is taken arbitrarily on the plane on which strain markers are observed. Let ϕ be the major-axis orientation of an ellipse (Fig. 1). Since a strain ellipse with the aspect ratio R results from the principal elongations $R^{1/2}$ and $R^{-1/2}$, $\log R^{1/2}$ equals the logarithmic strain and $\rho = \log R$ is the logarithmic quadratic strain or doubled natural strain. The double angle $\psi = 2\phi$ is theoretically more useful than ϕ. All ellipses are normalized by their area to have the value of π. Accordingly, unstrained state is represented by the unit circle.

Attributes of pre- and post-strain ellipses and strain ellipse are distinguished by the subscripts, 'i', 'f' and 's,' respectively. For example, ψ_s and ψ_f denote the doubled major-axis orientations of strain ellipse and final ellipse, respectively. ϕ_s indicates the maximum stretching orientation. Accordingly, the logarithmic quadratic strain of pre-, post-strain, and strain ellipses are referred to as ρ_i, ρ_f and ρ_s, respectively. Table 1 shows the symbols for important quantities.

3. Rationale for introducing hyperbolic geometry

Equations introduced by Dunnet (1969, Eq. 28) and Lisle (1985, Eq. A1.1) clearly show the connection between strain analysis and hyperbolic geometry. Dunnet derived the equation

$$\cosh \rho_i = \cosh \rho_f \cosh \rho_s - \sinh \rho_f \sinh \rho_s \cos\psi_f \qquad (1)$$

to relate the pre- and post-strain shapes of an elliptical strain marker to the strain ellipse, where the reference orientation is assumed to be parallel to the maximum elongation, i.e., $2\phi_s = \psi_s = 0$. In fact, Eq. (1) is termed the law of cosines in hyperbolic trigonometry, which relates the sides and interior angles of a triangle (Fig. 2) in a hyperbolic space (Ratcliffe, 2006). On the other hand Lisle (1985) shows an equation for the change in principal axes of an ellipse,

$$\sinh \rho_i \sin(\pi - \psi_i) = \sinh \rho_f \sin\psi_f \qquad (2)$$

This equation relates the sides to their opposite interior angles of the triangle (Fig. 2), and is called the law of sines in hyperbolic trigonometry.

Hyperbolic geometry gives a useful point of view for statistical processing of two-dimensional strains, because the geometry allows us to evaluate dissimilarity between strain ellipses. Once dissimilarity or distance between data is properly defined, data analysis can take advantage of various statistical techniques (e.g., Aitchison, 1986; Small, 1996; Duda et al., 2001; Egozcue et al., 2003; Sato and Yamaji, 2006; Yamaji and Sato, 2006). To illustrate this, suppose that we obtained many estimates of the strain ellipse from the assemblage of strain makers through bootstrap or some other
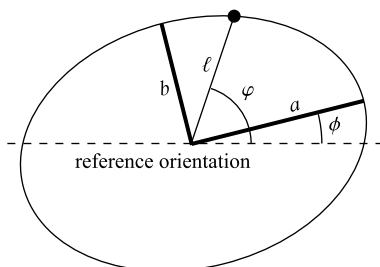
Table 1
List of important symbols

$\widehat{\mathbf{b}}$	Centroid of $\mathbf{b}^{(1)}, \ldots, \mathbf{b}^{(m)}$	Section 5.1.2
$\mathbf{b}^{(i)}$	Hyperbolic vector mean of the ith bootstrap sample	Section 5.1.2
C	Point on H^2 with the cartesian coordinates $(1, 0, 0)$	Fig. 4
∂D	Circle with the radius 1 on the plane $x_0 = 1$ and centered by C	Fig. 4
H^1	One-dimensional hyperbolic space, a special geodesic on H^2	Fig. 4
H^2	Two-dimensional hyperbolic space, the unit hyperboloid	Fig. 4
i, f, s	Subscripts for quantities of pre- and post-strain and strain ellipses, respectively	Section 2
ℓ	Moving radius of ellipse	Fig. 1
m	Number of bootstrap sample sets	Section 5.1.2
R	Aspect ratio of ellipse	Fig. 1
$\mathbf{v}$	Pole vector for defining a geodesic on H^2	Section 4.3
W_k	Kinematic vorticity number	Section 4.3
W_m	Mean kinematic vorticity number	Section 5.2
$\mathbf{x}$	Position vector or point on H^2	Section 4.1, Eq. (9)
$\widehat{\mathbf{x}}_s$	Hyperbolic vector mean	Eq. (20)
x_0, x_1, x_2	Cartesian coordinates	Fig. 4
(ζ, θ)	Radial and tangential components on the azimuthal projection of H^2	Section 4.4
λ	Resultant vector	Eq. (21)
ϕ	Major-axis orientation of ellipse	Fig. 1
φ	Angular coordinate used with ℓ	Fig. 1
ρ	Logarithm of R, logarithm of quadratic strain	Section 2
r, ψ, x_0	Cylindrical coordinates	Fig. 4
ϱ	Hyperbolic distance from the point C on H^2	Section 4.2
$\circ$	Hyperbolic inner product	Eq. (4)
$\|\|\|$	Hyperbolic vector length	Eq. (5)

resampling techniques. Then, how can we quantify the variation of the ellipses to estimate the uncertainty of the mean strain ellipse? Definition of the spread requires a measure, i.e., distance or dissimilarity between ellipses. If ellipses have large variations in their R and ϕ values, the spread is judged to be large and the mean has a large uncertainty. So, our question becomes what is the appropriate definition of a parameter space, in which a point has a one-to-one correspondence to the paired data R and ψ. In addition, the space requires an essential attribute: distance in the space should be equal to a strain measure needed to transform one ellipse to another. The conventional R_f/ϕ plot is not appropriate for this purpose. Open circles in Fig. 3 indicate two ellipses with the same aspect ratio and different orientations. Diamonds in this figure denote ellipses with a low aspect ratio. Distance between the circles is the same with that between the diamonds on this plot. However, the fat ellipses are much more alike to each other than the thin ellipses. Difference in ϕ is more significant for thin ellipses than for fat ones, but those distances are the same on this plot. It is unclear
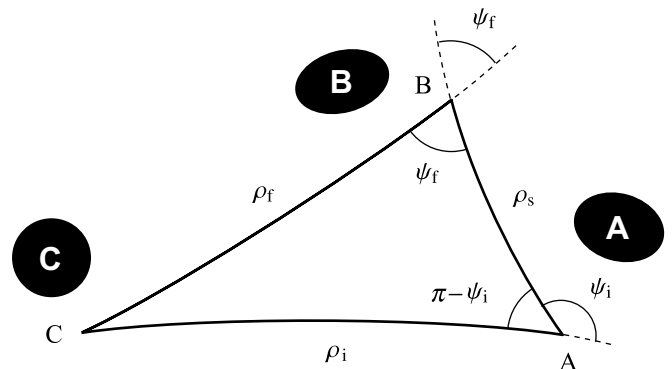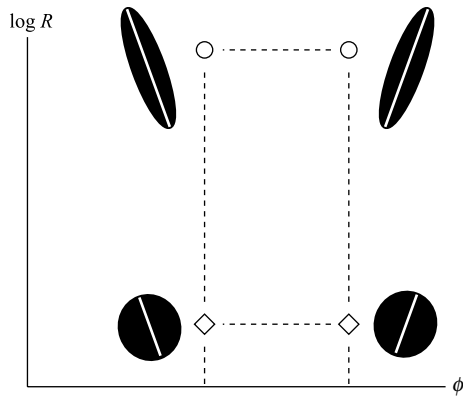

Fig. 2. Schematic illustration showing a hyperbolic triangle ABC, the vertices of which represent the ellipses A, B and C in physical space. Sides of the triangle are geodesics, the shortest paths connecting the vertices. The symbols ρ_f, ρ_i and ρ_s denote lengths of the sides.

Fig. 1. Ellipse with aspect ratio $R = a/b$ and major-axis orientation φ. The polar coordinates ℓ and ϕ denote a point on the ellipse.

Fig. 3. Conventional R/φ plot. Open circles and diamonds denote the points on the plot corresponding to black ellipses. R and φ are the aspect ratio and major-axis orientation of an ellipse, respectively.

whether the dissimilarity between the thin ellipses is larger than that between the elongate and circular ones with the same orientations.

The hyperbolic triangle in Fig. 2 not only suggests the connection between strain analysis and hyperbolic geometry, but also indicates that the hyperbolic space fills the statistical necessity. That is, the distances ρ_i, ρ_f and ρ_s equal the logarithmic quadratic strains needed to transform one ellipse to another denoted by the vertices of the triangle.

4. Hyperboloid model

Hyperbolic space is an abstract non-Euclidean space, and there are a few methods of visualizing the space. However, all the methods have distortion like cartographic projections of the globe. Among them we use the curved surface, called the unit hyperboloid, for the ease of statistical processing. The hyperboloid gives a useful visual expression of hyperbolic space at the cost of loosing the important attribute of this space, i.e., the constant curvature of -1. The content of the next two subsections are found in Reynolds (1993), Nakaoka (1993) and Ratcliffe (2006). The notation of this article basically follows that of Reynolds (1993).

4.1. The unit hyperboloid

The Cartesian coordinates $O\text{-}x_0x_1x_2$ is used throughout of this paper, where O is the coordinate origin. Then, the unit hyperboloid is defined by the equation,

$$-x_0^2 + x_1^2 + x_2^2 = -1 \tag{3}$$

In this article, only the upper half space $x_0 \geq 0$ is considered. The symbol H^2 refers to this surface (Fig. 4). We use the cylindrical coordinates $O\text{-}r\psi x_0$ as well, where r is the radial coordinate, ψ is the angular coordinate, and x_0 is the high along the cylinder axis. The Cartesian and cylindrical coordinates have the origin in common. H^2 has axial symmetry about the x_0-axis, and has a round base at the point C with the Cartesian coordinates $(1, 0, 0)$. It follows that H^2 has the expression $x_0 = \sqrt{r^2 + 1}$, and has hyperbolic profiles. H^1 is the hyperbola defined by the intersection of H^2 and the x_0x_1-plane.

Instead of the familiar definition of vector inner product in the Euclidean space, the inner product is defined as

$$\mathbf{a} \circ \mathbf{b} = -a_0 b_0 + a_1 b_1 + a_2 b_2 \tag{4}$$

which is called hyperbolic inner product. Position vectors are defined as usual: their initial point is fixed at the origin O.
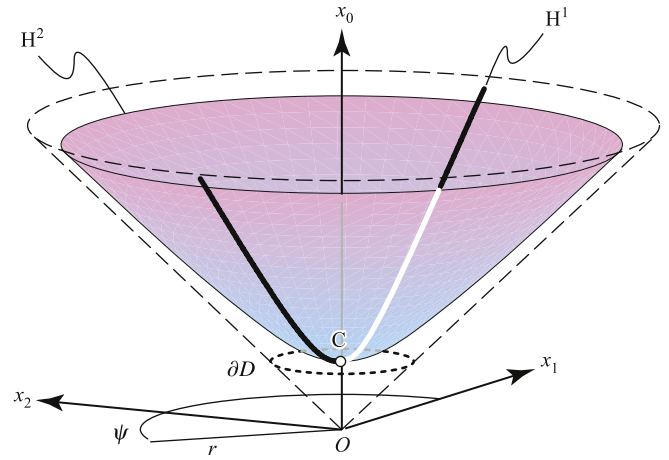
Fig. 4. The hyperboloid H^2 defined by Eq. (3) for visualizing hyperbolic geometry. Cartesian and cylindrical coordinates, $O\text{-}x_0x_1x_2$ and $O\text{-}r\psi x_0$, have the origin O in common. Intersection of H^2 and the x_0-axis defines the point C, which has the Cartesian coordinates $(1, 0, 0)$. This point represents the unit circle in the physical space, and other points on H^2 represent different ellipses with different combinations of R- and φ-values. Thick line H^1 is the geodesic defined by the intersection of H^2 and the x_0x_1-plane. Dotted line ∂D indicates the circle $x_1^2 + x_2^2 = 1$ in the plane $x_0 = 1$. Dashed lines show the cone that has its apex at the origin and includes ∂D. The hyperboloid asymptotically approaches the cone.

Accordingly, they are identified with their end points, and points are denoted by position vectors. In terms of a position vector $\mathbf{x}$, the cone $x_0 = r$ illustrated in Fig. 4 is written as $\mathbf{x} \circ \mathbf{x} = 0$. It is known that the inner product of the position vectors $\mathbf{a}$ and $\mathbf{b}$ with the endpoints above the cone is non-positive in sign, $\mathbf{a} \circ \mathbf{b} \leq 0$ (Ratcliffe, 2006, p. 56).

4.2. Distances, geodesics and translations on H^2

In terms of a position vector $\mathbf{x}$, H^2 is expressed as $\mathbf{x} \circ \mathbf{x} = -1$. Compared to the equation of the unit sphere, $\mathbf{x} \cdot \mathbf{x} = 1$ and considering the curvature -1 over the entire surface, H^2 is sometimes called a pseudosphere with the radius of $\sqrt{-1}$ (Vilenkin, 1968). Accordingly, spherical geometry and spherical statistics are useful guides for our study.

Given two points on H^2, the geodesic between the points is the shortest path on H^2. This is analogous to a great circle, which is the intersection of a plane through the origin and the sphere. Likewise, a geodesic on H^2 is defined by the intersection of a plane through the origin and H^2. H^1 is a geodesic through the point C, and is defined by the intersection of the x_0x_1-plane and H^2 (Fig. 4). Accordingly, a geodesic can be identified with the vector $\mathbf{v}$ perpendicular to the intersecting plane.

Length of the vector $\mathbf{x}$ is given by

$$\|\mathbf{x}\| = \sqrt{-\mathbf{x} \circ \mathbf{x}} \tag{5}$$

Due to the minus sign, the right-hand side of this equation is real for position vectors if their end points exist in the region above the cone. Distances on H^2 are measured along geodesics. That is, the distance between the points $\mathbf{a}$ and $\mathbf{b}$ upon H^2 is calculated by

$$d_H = \cosh^{-1}(-\mathbf{a} \circ \mathbf{b}) \tag{6}$$

analogous to the great-circle distance on the unit sphere expressed as $\cos^{-1}(\mathbf{a} \cdot \mathbf{b})$. It follows from Eqs. (4) and (6) that $\cosh^{-1} x_0$ is the distance between C and $\mathbf{x} = (x_0, x_1, x_2)^T$ on H^2. Let us use the symbol ϱ to refer to this distance. Then, we have

$$x_0 = \cosh \varrho = \frac{1}{2}\left(R + \frac{1}{R}\right) \tag{7}$$

H^2 can be written in the cylindrical coordinates as $x_0 = \sqrt{r^2 + 1}$. Combining this and Eq. (7) we obtain

$$r = \sinh \varrho = \frac{1}{2}\left(R - \frac{1}{R}\right). \tag{8}$$

Therefore, C-$\varrho\psi$ can be used as a coordinate system on H^2 with the origin at C (Fig. 4). This is sometimes called hyperbolic spherical coordinates (Barndorff-Nielsen, 1987). A point on H^2 can be expressed as

$$\mathbf{x}(\varrho, \psi) = (\cosh \varrho, \sinh \varrho \cos\psi, \sinh \varrho \sin\psi)^T \tag{9}$$

Just as translation or movement of a rigid body on the unit sphere is described by a Euler rotation which is further denoted by an orthogonal matrix, translation on H^2 is expressed by a hyperbolic orthogonal matrix with the determinant 1. If the translation is along the geodesic that is defined by a plane containing the x_0-axis, the matrix has the form

$$\mathbf{Q}(\varrho, \psi) = \begin{pmatrix} 1 & 0 & 0 \\ 0 & \cos\psi & -\sin\psi \\ 0 & \sin\psi & \cos\psi \end{pmatrix} \begin{pmatrix} \cosh\rho & \sinh\rho & 0 \\ \sinh\rho & \cosh\rho & 0 \\ 0 & 0 & 1 \end{pmatrix}$$
$$\times \begin{pmatrix} 1 & 0 & 0 \\ 0 & \cos\psi & \sin\psi \\ 0 & -\sin\psi & \cos\psi \end{pmatrix} \tag{10}$$

where ψ denotes the direction of translation.

Translation does not change distances between points so that any figure defined by a set of points does not change its shape and size on H^2. Consider the congruent triangles ABC and A′B′C′ in Fig. 5; A′ coincides with C and sides AC and A′C′ are on H^1. They have the sizes a, b and c, and the opposite interior angles α, β and γ. The translation along H^1 from A′B′C′ to ABC is denoted by $\mathbf{Q}(-b, 0)$. The apices B and B′ are denoted by the vectors $\mathbf{x}(B) = (\cosh a, \sinh a \cos\gamma, \sinh a \sin\gamma)^T$ and $\mathbf{x}(B') = (\cosh c, \sinh c \cos(\pi - \alpha), \sinh c \sin(\pi - \alpha))^T$. These vectors are related through an orthogonal matrix as

$$\begin{pmatrix} \cosh c \\ \sinh c \cos(\pi - \alpha) \\ \sinh c \sin(\pi - \alpha) \end{pmatrix} = \begin{pmatrix} \cosh b & -\sinh b & 0 \\ -\sinh b & \cosh b & 0 \\ 0 & 0 & 1 \end{pmatrix}$$
$$\times \begin{pmatrix} \cosh a \\ \sinh a \cos\gamma \\ \sinh a \sin\gamma \end{pmatrix}.$$

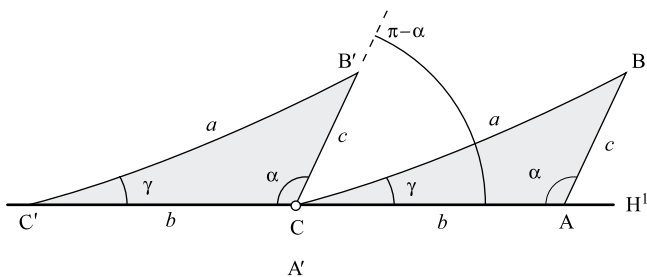Extracting the first and third rows of the both sides of this equation, we have

$$\cosh c = \cosh b \cosh a - \sinh b \sinh a \cos\gamma \tag{11}$$

and

$$\sinh c \sin(\pi - \alpha) = \sinh a \sin\gamma \tag{12}$$

These are the cosine and sine laws of hyperbolic trigonometry. Replacing a, b, c, α and γ by ρ_f, ρ_s, ρ_i, ψ_i and ψ_f, respectively, Eqs. (11) and (12) becomes Eqs. (1) and (2). Consequently, formulas of strain analysis correspond to those of hyperbolic trigonometry.

The above correspondence demonstrates that the deformation of elliptical objects in the physical space is denoted by a translation of this kind on H^2. In addition, ϱ equals ρ, meaning that the strain needed to make one ellipse to another equals the geodesic distance between the points representing the ellipses. Consequently, H^2 has ideal properties as the parameter space for dealing with R_f/ϕ data.

As a result, deformation in the physical space is simply denoted by the linear transformation of hyperbolic vectors such that

$$\mathbf{x}\left(\rho_f, \psi_f\right) = \mathbf{Q}(\rho_s, \psi_s)\mathbf{x}(\rho_i, \psi_i) \tag{13}$$

where $\mathbf{x}$ and $\mathbf{Q}$ has been defined in Eqs. (9) and (10). As the strain ellipse is represented by a point $\mathbf{x}_s$ on H^2, Eq. (13) is rewritten as

$$\mathbf{x}_f = \mathbf{Q}(\mathbf{x}_s)\mathbf{x}_i \tag{14}$$

Eq. (13) is simplified to

$$\mathbf{x}\left(\rho_f, \psi_f\right) = \begin{pmatrix} \cosh \rho_i \cosh \rho_s \\ \cosh \rho_i \sinh \rho_s \\ \sinh \rho_s \end{pmatrix} \tag{15}$$

for the translation along H^1 of the points with the initial hyperbolic spherical coordinates $(\rho_i, \pi/2)$. Eq. (15) denotes the curve with the variable ρ_s that keeps the constant distance ρ_i from H^1, analogous to the relationship of a small and great circle on a sphere.

4.3. General shear

Various deformation types in the physical space are distinguished by the kinematic vorticity number W_k (e.g., Ramberg, 1975; De Paor, 1993; Passchier and Trouw, 2005), which has values 0, 1 and >1 for pure, simple and super shear, respectively. W_k is not defined in terms of deformations, but of the velocity field resulting in those deformations. That is, W_k is the ratio of asymmetric and symmetric parts of velocity gradient tensor $\mathbf{L}$ (Truesdell, 1954), which is related to the deformation gradient tensor $\mathbf{F}$ and its material derivative $\dot{\mathbf{F}}$ via the equation $\mathbf{L} = \dot{\mathbf{F}}\mathbf{F}^{-1}$ (Chadwick, 1999, p. 65). $\mathbf{L}$ and $\mathbf{F}$ are different quantities even for a steady flow. However, W_k has a qualitative relationship with the hyperboloid model as follows.

In analogy with small circles on a sphere, there are three kinds of curves on H^2 (Reynolds, 1993), each of which corresponds to a type of deformation in the physical space. The curves are defined by the intersection of planes and H^2 so that a point $\mathbf{x}$ on such a curve satisfies the linear equation

$$\mathbf{x} \circ \mathbf{V} = -\kappa \tag{16}$$

Those curves are termed 'cycles' in hyperbolic geometry. The vector $\mathbf{v}$ is called the pole of the plane, indicating the attitude of the plane and κ indicates the position of the plane. Planes with $\kappa = 0$ include the origin O so that the curves defined by those planes are geodesics.

4.3.1. Pure shear

Pure shear has been explained in the previous subsection: such a deformation carries points on H^2 along a geodesic on the planes

Fig. 5. Congruent triangles ABC and A′B′C′ on H^2. The triangles have the apices C and A′ at the same point. C is the point where the x_0-axis meets H^2 (Fig. 4). Sides of the triangles have the lengths a, b and c. The side b is on H^1.

parallel to the x_0-axis or along a line that keeps a constant hyperbolic distance from such a geodesic (Fig. 6). The curve shown by Eq. (15) is the one along H^1, and is regarded as the 'strain path' of an initial ellipse represented by a point on the curve for the growing strain increasing with ρ_s. Those planes have a common pole vector $\mathbf{v}$ lying on the x_1x_2-plane. In this case, the pole vector satisfies $\mathbf{v} \cdot \mathbf{v} > 0$ (Reynolds, 1993). And, the W_k value is 0, equivalent to the ratio v_0/v_r of the cylindrical components of the vector $\mathbf{v}$.

4.3.2. General shear between pure and simple

General shear between pure and simple has strain paths on the intersection of H^2 and the plane defined by the pole vectors between the x_1x_2-plane and the cone in Fig. 4. This case is considered in detail for kinematic vorticity analysis in Section 5.2. The geodetic corresponding to this vector is asymptote to the cone in the two different directions ψ_1 and ψ_2 in Fig. 7, corresponding to the fact that the straining and destraining of an ellipse leads to ellipses with different stretching orientations in physical space. In this case, we have $0 \leq W_k \leq 1$, concordant to the range of the ratio v_0/v_r.

Regarding kinematic vorticity analysis (Section 5.2), the fabric attractor (flow plane) is represented by a geodetic on H^2, and the ratio v_0/v_r of the geodetic is exactly equal to the mean kinematic vorticity number (Appendix B).

4.3.3. Simple shear

The strain path of simple shear is represented by a 'horocycle' on H^2, i.e., a curve lying on a plane with $\mathbf{v}$ tangent to the cone in Fig. 4. This vector satisfies $\mathbf{v} \cdot \mathbf{v} = 0$. As a result, the curves are parabolic on H^2 (Fig. 8). A horocycle is asymptote to the same point at infinity, corresponding to the fact that infinite simple shear results in an infinitely long and thin ellipse irrespective of the sense of shear. Horocycles in Fig. 8 are asymptote to H^1 in the $+x_1$ direction. In this case, the value of W_k equals 1. This is equivalent to the ratio of the cylindrical coordinates of the vector v_0/v_r.

4.3.4. Super shear

Super shear or super simple shear is characterized by W_k values greater than 1, and is the behavior of fluid inclusions immersed in
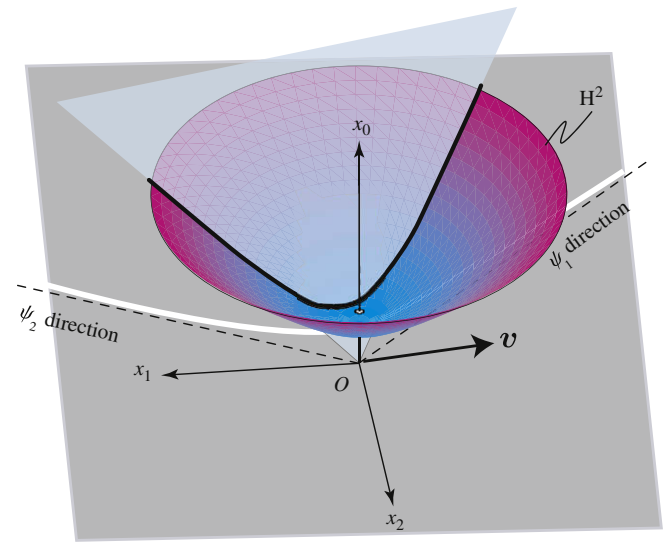
a fluid with different viscosity subject to shearing (e.g., De Paor, 1983; Mulchrone and Walsh, 2006). Those inclusions change their aspect ratios and orientations synchronously. Such a behavior is illustrated by a circular orbit on H^2 (Fig. 9). The orbit lies on a plane with $\mathbf{v}$ included by the cone. In this case, the pole vector satisfies $\mathbf{v} \cdot \mathbf{v} < 0$ (Reynolds, 1993). The range of W_k is concordant with that of the ratio v_0/v_r.

4.3.5. Rigid-body rotation

Rigid-body rotations in the physical space are represented by the circular orbits on the planes perpendicular to the x_0-axis, i.e., $\mathbf{v} = 1$. Rigid-body rotations has the value $W_k = \infty$, concordant with $v_0/v_r = \infty$.

4.4. Cartography

Projections from H^2 onto a Euclidean plane are convenient tools for investigating spatial data on H^2, although the projections
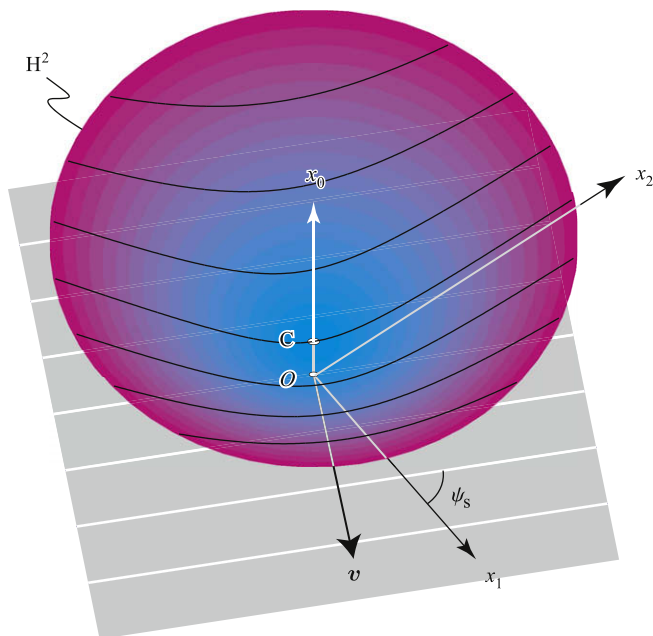

Fig. 7. Geodesic (thick line) on H^2 lying on a plane through the origin. The plane has the pole vector $\mathbf{v}$ between the x_1x_2-plane and the cone in Fig. 4. White line is the orthogonal projection of the geodesic onto this plane.

Fig. 6. Solid lines showing the curves on H^2 corresponding to the strain paths of coaxial strain. White lines on the x_1x_2-plane are the orthogonal projections of the curves.
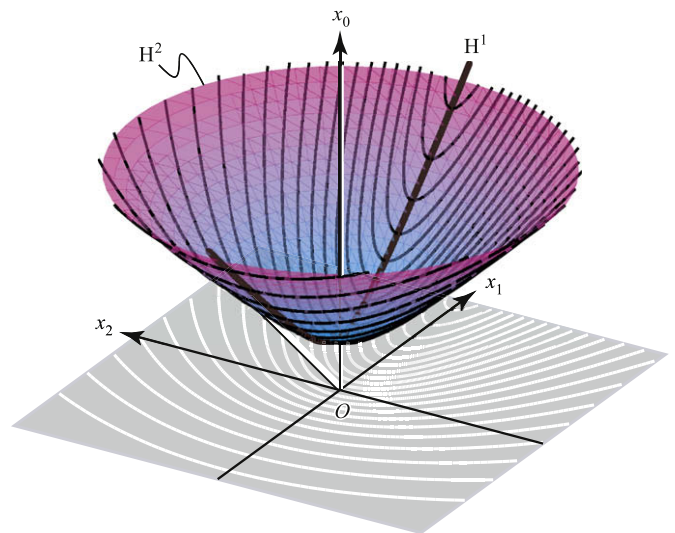

Fig. 8. The horocycles (thin lines) on H^2 that are defined by the intersections of H^2 and the planes with the pole vector $\mathbf{v}$ tangent to the cone in Fig. 4. Those curves represent strain paths for simple shear in the reference orientation. White lines on the x_1x_2-plane show the orthogonal projections of the horocycles.

inevitably have distortion like those from the globe onto a plane. Consider the mapping from a point with polar coordinates (ρ, ψ) on H^2 to the polar coordinates (ζ, θ) on the Euclidean plane (Fig. 10). We consider only azimuthal projections, meaning that $\theta = \psi$. All the projections in this subsection preserve azimuths from C to any point on H^2, but the conventional R_f/ϕ plot (Fig. 3) does not.

4.4.1. Equal-area projection
The projection denoted by the equation

$$\zeta = 2\sinh(\rho/2) = R^{1/2} - R^{-1/2} \qquad (17)$$

preserves areas (Reynolds, 1993), meaning that the area of any closed region on H^2 equals that of the corresponding region on the plane (Fig. 11). $(R^{1/2} - R^{-1/2})$ is the diameter of the Mohr circle of strain (Brace, 1961). This projection is useful for displaying the variation of ellipses, because the variation is visualized by the dispersion of data points on H^2. The area preservation guarantees that density of points on H^2 is preserved on this map. Straining of ellipses in the physical space corresponds to the translation of points on H^2, which does not affect their density. So, the points indicating pre- and post-strain ellipses have the same dispersion on this map. For this reason, this projection gives the best visualization for the dispersion of R_f/ϕ data.

4.4.2. Gnomonic projection
Gnomonic projection transforms a point on H^2 along a line through the origin O onto the disk that is denoted by $x_0 = 1$ and $x_1^2 + x_2^2 < 1$. Points on the fringe of this disk (∂D in Fig. 4) represent points at infinity, and the entire surface of H^2 is mapped onto the disk (Fig. 12). This projection has the expression,

$$\zeta = \tanh \rho = \left(R^2 - 1\right) / \left(R^2 + 1\right) \qquad (18)$$

where $0 \leq \zeta < 1$ (Fig. 10). Geodesics on H^2 are mapped to straight lines on the disk. A horocycle (Fig. 8) is mapped to an ellipse that inscribes ∂D. Specifically, a horocycle through C is shown on this projection by a circle.

This projection is convenient for determining the mean kinematic vorticity number (Section 5.2). The plot by Jessup et al. (2007) was devised for this purpose, and takes $\tanh \rho$ and ϕ as rectangular Cartesian coordinates instead of the polar coordinates of the gnomonic net proposed in this article.
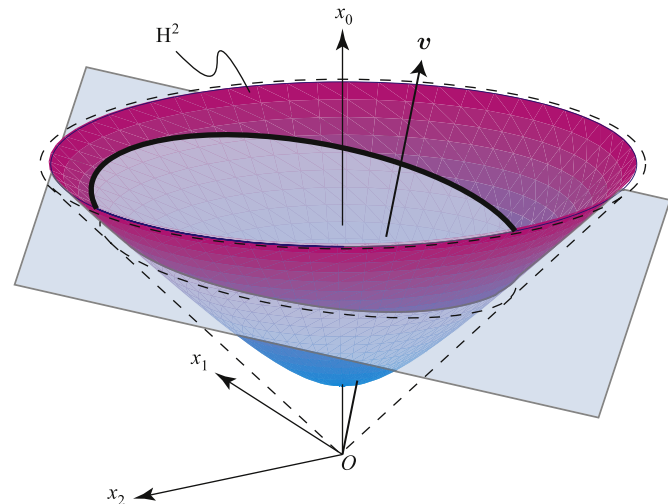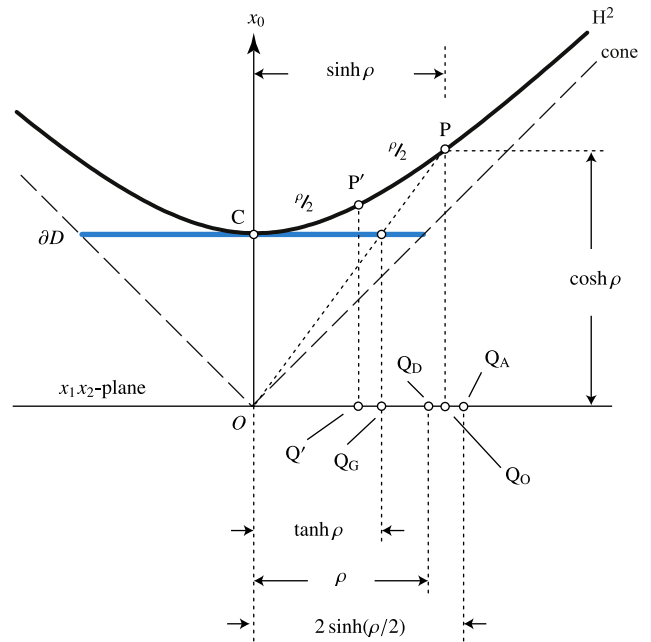

Fig. 10. Section of H^2 through the x_0-axis for illustrating projections from H^2 onto the Euclidean x_1x_2-plane. The hyperbolic distance of P from C is ρ, and P′ is the midpoint. Q′ is the orthogonal projection of P′, and is the midpoint of the segment between O and Q_A. The points Q_G, Q_D, Q_O and Q_A are the gnomonic, equidistant, orthographic and equal-area projection of P, respectively. Dashed lines indicate the cone in Fig. 4.

4.4.3. Equidistant projection
The plot of Elliott (1970) is the equidistant projection of H^2, and has the relationship $\zeta = \rho = \log R$. In spite of the adjective 'equidistant,' distances on the map is correct only from the map center C. Distances between other points are not. The name of this projection is used by Reynolds (1993) to emphasize the correspondence to the equidistant projection of the globe.

Fig. 9. Solid line on H^2 showing the orbit corresponding to super shear. The orbit lies on the plane with the pole vector **v**. Dashed line shows the cone in Fig. 4.
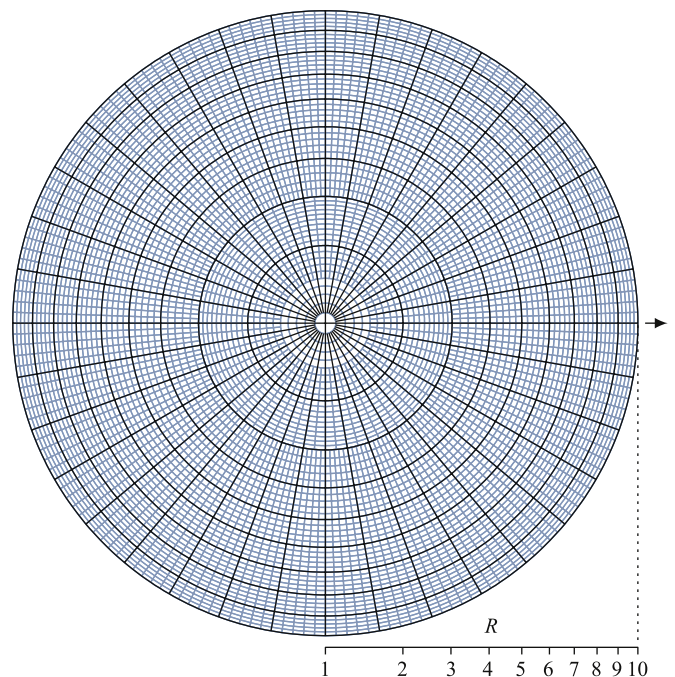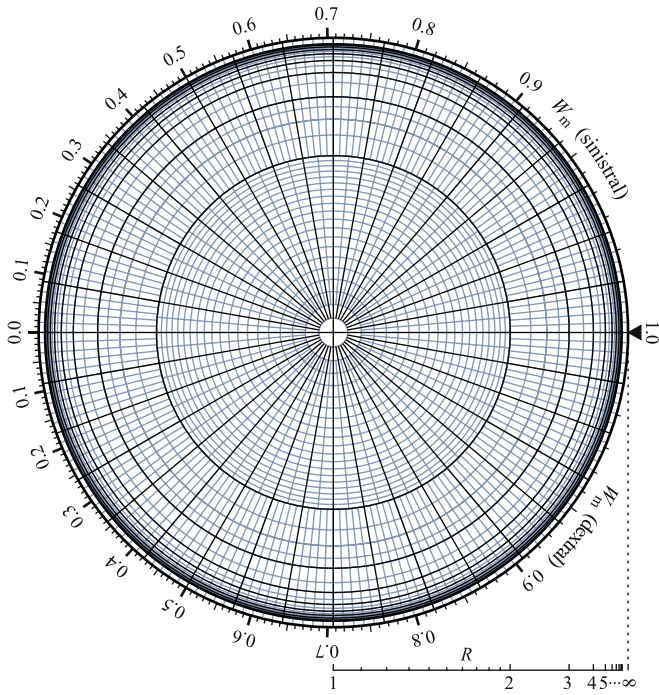

Fig. 11. Equal-area net of H^2. Radial lines and concentric circles are iso-R and φ lines, respectively, for indicating the shapes and orientations of ellipses. Radius of the circles are given by Eq. (17). Center of this net corresponds to the point C in Fig. 4, and arrow indicates the reference orientation.

Fig. 12. Gnomonic net of H^2. Center of this net corresponds to the point C on H^2, and triangle indicates the reference orientation. Eq. (18) gives the radii of iso-R circles. Mean kinematic vorticity number W_m can be determined with this net (Section 5.2). The outermost circle with tick marks indicate ∂D in Fig. 4, points on which represent ellipses with $R = \infty$. Decimals attached on the marks indicate the kinematic vorticity number by Eq. (A5).

This projection is useful, if one needs the directions and distances of points from a specific location on H^2. In this case, the location along with the points to the point C on H^2 using Eq. (14). Then, the equidistant projection of the points shows the directions and distances from the specified location to the original points. This method is used in Section 5.2 for error estimation of R_f/ϕ strain analysis. The hyperbolic net of De Paor (1988) is a variant of this projection in that the hyperbolic net uses the angle ϕ (Fig. 1), instead of the double angle ψ, as the tangential components.

4.4.4. Orthographic projection

The plot by Wheeler (1984) is the orthographic projection of H^2, i.e., the orthogonal projection onto the x_1x_2-plane. This projection is denoted by the equation, $\zeta = \sinh \rho$ (Eq. (8)). It is the strong point of this projection that strain paths for coaxial strain are expressed by parallel lines on the plot. The trend of the lines corresponds to the maximum stretching axis in the physical space. Therefore, it is easy to see if an ellipse can be transformed from another by strains with a prescribed stretching axis.

5. Strain analysis

Aspect ratios and orientations of pre- and post-strain ellipses are related to each other by a couple of complicated equations (Ramsay, 1967, p. 205–9). By means of hyperbolic geometry, this relationship is simplified to the linear transformation in Eq. (13). And, the theories of two-dimensional strain analysis are simplified as well. We consider a few of them in this section.

5.1. Coaxial strain determined from R_f/ϕ data

First, we consider the determination of coaxial strain from R_f/ϕ data obtained from elliptical strain markers such as pebbles (Flinn, 1956; Hossack, 1968) and ooids (Cloos, 1947) or from non-elliptical

fossils (e.g., Lisle, 1985) observed on a section of a deformed rock. A homogeneous deformation of the markers and their matrix is assumed as usual. It is shown that the confidence region of inferred strain is easily obtained in our formulation.

Suppose that we observed n elliptical strain markers, and that the shape and orientation of the markers are transformed into the data points $\mathbf{x}_f^{(1)}, \ldots, \mathbf{x}_f^{(n)}$ on H^2 via Eq. (9). Here, our task is to determine the point $\mathbf{x}_s$ indicating the optimal strain for the data and its error.

5.1.1. Hyperbolic vector mean

To determine the optimal strain, we make a simple assumption for the pre-strain distribution of the points $\{\mathbf{x}_i^{(1)}, \ldots, \mathbf{x}_i^{(n)}\}$. That is, the points have the centroid at the point C on H^2. This is denoted by the equation,

$$[\mathbf{x}_i^{(1)} + \cdots + \mathbf{x}_i^{(n)}] / \| \mathbf{x}_i^{(1)} + \cdots + \mathbf{x}_i^{(n)} \| = (1, 0, 0)^T. \tag{19}$$

Note that strain is denoted by translation upon H^2, and the translation does not affect distances between points on H^2. It follows that, on the one hand, the strain that carries $\{\mathbf{x}_i^{(1)}, \ldots, \mathbf{x}_i^{(n)}\}$ to $\{\mathbf{x}_f^{(1)}, \ldots, \mathbf{x}_f^{(n)}\}$ transforms the centroid of the former set to that of the latter. On the other hand, the point C represents the unit circle in the physical space, and the strain ellipse is the result of strain from the unit circle. Therefore, the latter centroid coincides with the point on H^2 that represents the strain ellipse. Determination of the optimal strain is surprisingly simple in the present formulation: the strain for the data is represented by the mean,

$$\widehat{\mathbf{x}}_s = \boldsymbol{\lambda} / \| \boldsymbol{\lambda} \|, \tag{20}$$

where

$$\boldsymbol{\lambda} = \mathbf{x}_f^{(1)} + \cdots + \mathbf{x}_f^{(n)} \tag{21}$$

and $\| \boldsymbol{\lambda} \|$ are termed the resultant vector and the resultant length of data vectors, respectively (Jensen, 1981). The same terms are used in spherical statistics (Mardia, 1972; Mardia and Jupp, 1999). It is straightforward to take into account measurement errors of data. The weighted mean

$$\widehat{\mathbf{x}}_s = \frac{w^{(1)}\mathbf{x}_f^{(1)} + \cdots w^{(n)}\mathbf{x}_f^{(n)}}{\left\| w^{(1)}\mathbf{x}_f^{(1)} + \cdots w^{(n)}\mathbf{x}_f^{(n)} \right\|}$$

deals with those data, where $w^{(i)}$ is the weight of the ith datum.

Once the optimal point $\widehat{\mathbf{x}}_s$ is obtained, the corresponding ρ- and ψ-values are calculated by the inverse of Eq. (9). That is,

$$\rho = \cosh^{-1} x_0 = \log\left(x_0 + \sqrt{x_0^2 - 1}\right) \tag{22}$$

$$\psi = \text{atan2}(x_2, x_1) \tag{23}$$

where atan2(x_2, x_1) denotes the arctangent of x_2/x_1 and has the range $(-\pi, \pi]$ corresponding to the quadrant of the x_1x_2-plane. In this way, the optimal values $\widehat{\rho}_s$, $\widehat{\psi}_s$, $\widehat{R}_s = \exp(\widehat{\rho}_s)$ and $\widehat{\phi}_s = \widehat{\psi}_s/2$ are derived from $\widehat{\mathbf{x}}_s$.

5.1.1.1. Example 1.
The method of hyperbolic vector mean was tested, first, with the natural R_f/ϕ data from the photomicrograph of 282 deformed ooids in Ramsay and Huber (1983). The data were transformed into position vectors $\mathbf{x}_f^{(1)}, \ldots, \mathbf{x}_f^{(282)}$ via Eq. (15), and the hyperbolic vector mean was calculated using Eqs. (20) and (21). As a result, I obtained the optimal values, $\widehat{R}_s = 1.50$ and $\widehat{\phi}_s = -46.9°$ (Fig. 13), which are included by the 95% confidence intervals

$\widehat{R}_s = 1.51 \pm 0.06$ and $\widehat{\phi}_s = -46.9° \pm 2.3°$ determined by the method of Yamaji (2005).

5.1.1.2. Example 2. The second data set is artificial for simulating R_f/ϕ data deformed from fossils, which are not necessarily elliptical. The graphical method of Wellman (1962) is usually employed to estimate strain from such fossils, but R_f/ϕ data can be obtained from the ellipses inscribing rectangles that are fitted on certain parts of the fossils (Fig. 14a) (Lisle, 1985). A specific part of fossils has a certain shape with individual variation to some extent if the fossils belong to one paleontological taxon. Accordingly, the ellipses abstracted from that part have a narrow range of R_i values. The artificial data in Fig. 14b were generated with the parameters $R_s = 2$ and $\phi_s = 0$ to simulate such a data set. The present method yielded the solution, $\widehat{R}_s = 2.000$ and $\widehat{\phi}_s = 0.000°$. That is, the optimal strain ellipse exactly coincided with the assumed one.

Theoretically, the present method is perfectly accurate, provided that pre-strain points had the centroid at C. Deviation of the centroid from C directly gives rise to the inaccuracy of the optimal solution. The artificial data in Fig. 14 were generated with the pre-strain points exactly at C. Therefore, the strain estimation was perfect. Uncertainty of the estimated strain comes from the finite number of data.

5.1.2. Error analysis

The bootstrap method (e.g., Davison and Hinkley, 1997) is employed to draw a confidence region of the optimal strain on H^2. Suppose that we observed n strain markers, from which n data are resampled with replacement to make $m = 10n$ bootstrap data sets. Then, by means of Eq. (20), the optimal solutions $\mathbf{b}^{(1)}, ..., \mathbf{b}^{(m)}$ are determined for the bootstrap data sets. The spread of those points around their centroid $\widehat{\mathbf{b}}$ indicates the uncertainty of the optimal solution $\widehat{\mathbf{x}}_s$ (Fig. 15). This centroid is obtained by Eqs. (20) and (21), where $\mathbf{x}_f^{(i)}$ in the latter equation is replaced by $\mathbf{b}^{(i)}$.

Following Michael (1987) who estimated the uncertainty of stresses obtained from focal mechanism data by means of bootstrap resampling, a confidence region of the optimal strain is defined as a closed region on H^2. Namely, if a 95% confidence region is required, the solutions $\mathbf{b}^{(1)}, ..., \mathbf{b}^{(m)}$ are sorted in ascending order of their distances from the centroid. Then, the confidence region is the polygon that contains only the first $0.95m$ solutions.

We consider a method for error estimation for the optimal strain determined from strain markers that may have significant pre-strain anisotropy expressed by the cluster of the points $\mathbf{x}_i^{(1)}, ..., \mathbf{x}_i^{(n)}$ with non-rotational symmetry around the point C on H^2. Sedimentary grain fabric has such anisotropy to some extent (Griffiths, 1967). That is, Potter and Pettijohn (1963, p. 44) pointed out that sedimentary particles often exhibit bimodal orientations separated by $\sim 90°$. This tendency is expressed by an eccentric cluster of data points centered by the point C on H^2 (Yamaji and Masuda, 2005). Other types of initial grain fabric, including strong imbrication, lead to inaccuracy of the present technique. Given the stretching orientation of the sediment, the method of De Paor (1988) can be employed to evaluate the strain from imbricated fabrics.

The artificial R_f/ϕ data in Fig. 14b have such asymmetry as described by Potter and Pettijohn (1963) and Yamaji and Masuda (2005). In those cases, cluster of the points $\mathbf{b}^{(1)}, ..., \mathbf{b}^{(m)}$ exhibits significant deviation from rotational symmetry about the point $\widehat{\mathbf{b}}$, and shows elongation similar to the cluster of the post-strain points $\mathbf{x}_f^{(1)}, ..., \mathbf{x}_f^{(m)}$. Dashed line in Fig. 15b shows an example. This line is elliptical on this figure, the eccentricity of which is due to the distortion of the equal-area projection. The region encircled by this line is a circle on H^2. However, the points $\mathbf{b}^{(1)}, ..., \mathbf{b}^{(m)}$ make an elliptical cluster on H^2. This is evidenced by the dots that are not enclosed by the dashed line in Fig. 15b. They are scattered out of the region depicted by the dashed line. To cope with the eccentric shape of the cluster on H^2, the confidence region of $\widehat{\mathbf{x}}_s$ drawn on H^2 should be an oval.

To meet the requirement above, the spread of $\mathbf{b}^{(1)}, ..., \mathbf{b}^{(m)}$ is evaluated by the Mahalanobis distances (Duda et al., 2001) from the cluster center $\widehat{\mathbf{b}}$ on H^2. For this purpose, this center along with the points is translated to the area around the point C on H^2 so that the new centroid coincides with this point and that the azimuthal equidistant projection can be used to estimate the azimuth and distance of points from their centroid. Then, the ith point moves to $\bar{\mathbf{b}}^{(i)} = [\mathbf{Q}(\widehat{\mathbf{b}})]^{-1}\mathbf{b}^{(i)}$ (Eq. (14)). Since the translation does not affect the relative positions between the points, the centroid of $\bar{\mathbf{b}}^{(1)}, ..., \bar{\mathbf{b}}^{(m)}$ exists at C. Then, the azimuthal equidistant projection of the points preserves the azimuths and distances of the points from C (Section 4.4.3). Let $\mathbf{y}^{(i)}$ be the projection of $\bar{\mathbf{b}}^{(i)}$. Then, the points $\mathbf{y}^{(1)}, ..., \mathbf{y}^{(m)}$ make a cluster at the center of equidistant chart. The covariance matrix (Johnson and Wichern, 2002),

$$\mathbf{c} = \frac{1}{m}\left\{\mathbf{y}^{(1)}\left[\mathbf{y}^{(1)}\right]^T + \cdots + \mathbf{y}^{(m)}\left[\mathbf{y}^{(m)}\right]^T\right\},$$
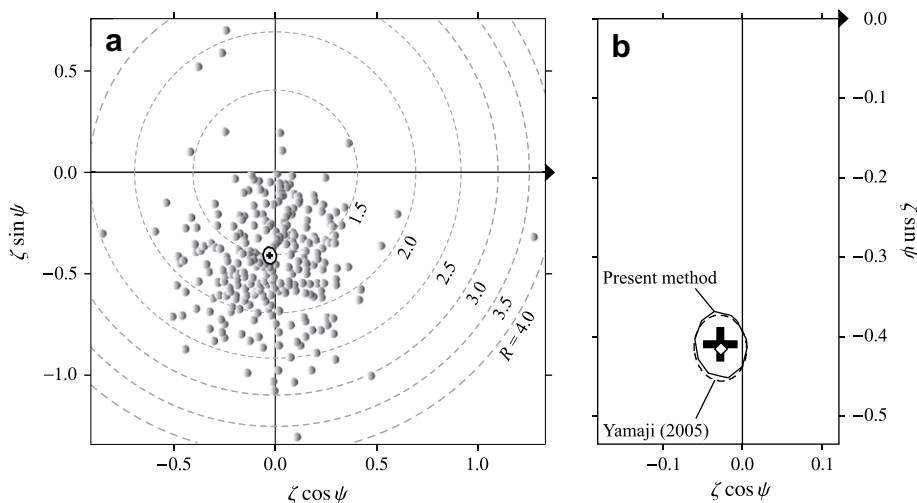

Fig. 13. (a) Equal-area projection (Section 4.4) showing the optimal strain (cross) and its 95% confidence region (polygon) determined by the present method for the R_f/ϕ data from the deformed ooids in (Ramsay and Huber, 1983, p. 83). Solid triangle indicates the reference orientation. The parameters ζ (Eq. (17)) and ψ are the polar coordinates of the equal-area projection. (b) Close-up of the 95% confidence regions and the optimal strains strains determined by the present and Yamaji's (2005) methods. Cross and diamond indicate the optimal solutions by the methods, respectively.
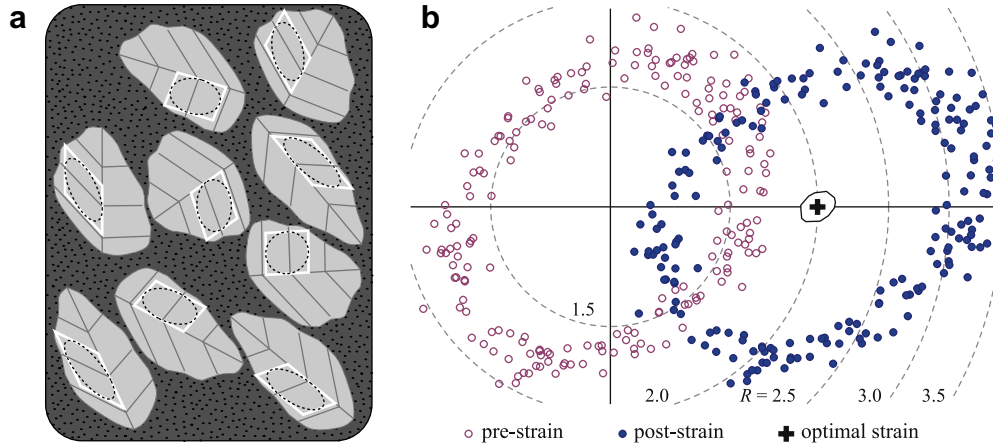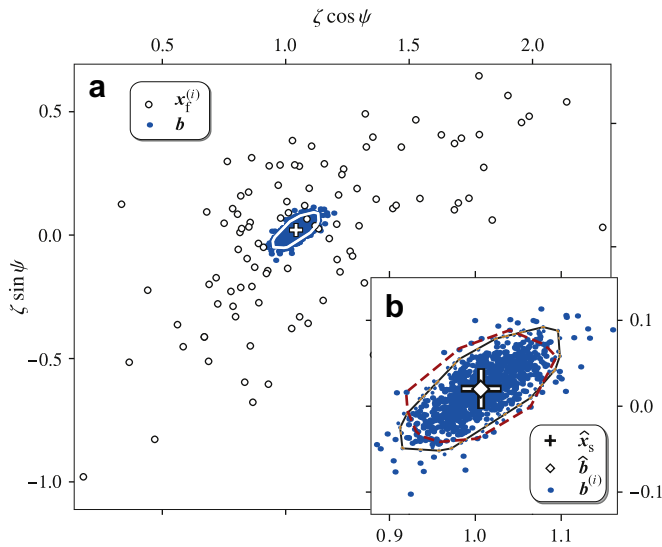
Fig. 14. Example of non-elliptical strain markers. (a) Schematic illustration showing deformed fossil leaves. Ellipses are fitted on parallelograms with the sides being parallel to specific veins. The ellipses give R_f/φ data. (b) Equal-area projection showing artificial data simulating the cases like (a). Points corresponding to 200 pre-strain ellipses have the centroid at the origin of this plot. Post-strain ellipses were generated from the pre-strain ones with the assumed strain, $R_s = 2$ and $\varphi_s = 0$. The pre-strain points have the centroid at C. Solid line centered by the cross denotes the 95% confidence region of the optimal strain ellipse.

characterizes the eccentric cluster shape, thereby the Mahalanobis distance of $\mathbf{y}^{(i)}$ from the center is written as $\sqrt{[\mathbf{y}^{(i)}]^T\mathbf{C}^{-1}\mathbf{y}^{(i)}}$. This distance is used as the key to sort the bootstrap solutions $\mathbf{b}^{(1)}, \ldots, \mathbf{b}^{(m)}$. Namely, the solutions are renumbered to have the ascending order of the Mahalanobis distances of $\mathbf{y}^{(1)}, \ldots, \mathbf{y}^{(m)}$. If we want to determine the (100α)% confidence region, the polygon enveloping only the points $\mathbf{b}^{(1)}, \ldots, \mathbf{b}^{(100\alpha m)}$ on H^2 approximates the confidence region of the optimal solution $\widehat{\mathbf{x}}_s$, where $0 < \alpha < 1$ (Fig. 15). For example, the value $\alpha = 0.95$ is used when 95% confidence region is required.

Once the confidence region is drawn on H^2, we use the method used by Yamaji (2005) to evaluate the confidence intervals of the optimal R- and φ-values. First, the circles that inscribe and circumscribe the confidence region are drawn on H^2 to determine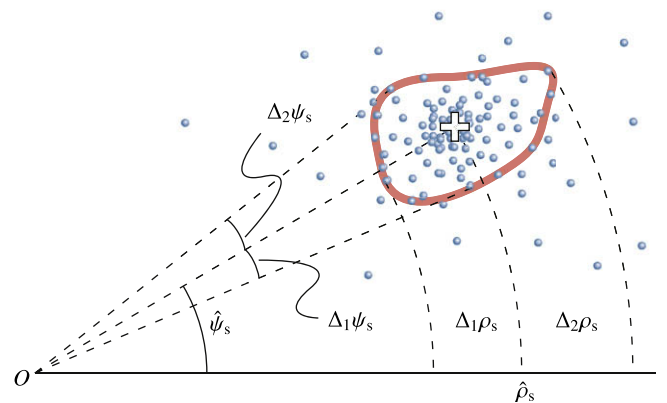 $\Delta_1\rho$ and $\Delta_2\rho$ (Fig. 16). The sector that has the apex at the origin with the smallest apical angle to include the region is also used to define

$\Delta_1\psi$ and $\Delta_2\psi$. The former pair is transformed into the lower and upper confidence limits for the optimal aspect ratio $\widehat{R}$ as $\exp(\widehat{\rho}_s - \Delta_1\rho)$ and $\exp(\widehat{\rho}_s + \Delta_2\rho)$, respectively. Those of the optimal major-axis orientation are $(\widehat{\psi}_s - \Delta_1\psi)/2$ and are $(\widehat{\psi}_s + \Delta_2\psi)/2$. If the confidence region includes the origin, these error bounds become indeterminate. The 95% confidence intervals for the example in Fig. 13 are $\widehat{R}_s = 1.50 \pm 0.06$ and $\widehat{\phi}_s = -46.9° \pm 2.6°$, largely identical with those of (Yamaji, 2005). The confidence intervals for the example in Fig. 14 are $\widehat{R}_s = 2.000^{+0.114}_{-0.108}$ and $\widehat{\phi}_s = 0.000°\,{}^{+2.167°}_{-2.157°}$. For the case of the data with strong anisotropy in Fig. 15, the optimal strain has the parameters, $\widehat{R}_s = 2.717^{+0.236}_{-0.219}$ and $\widehat{\phi}_s = 0.556°\,{}^{+1.806°}_{-2.071°}$.

5.2. Kinematic vorticity analysis

Rotational wakes of rigid particles are used to infer the vorticity of the paleo flow field in sheared rocks. Specifically, kinematic vorticity analysis estimates the kinematic vorticity compatible with those flow patterns (e.g., Ghosh and Ramberg, 1976; Means et al., 1980; Passchier and Simpson, 1986; Passchier, 1987; Wallis et al., 1993; Wallis, 1995; Simpson and De Paor, 1997). The gnomonic projection gives a simple graphical technique to solve this problem.

Assuming that particle shapes are approximated by ellipses with the aspect ratio $R = \exp(\rho)$ and that the flow field is the superposition of simple and pure shears, Bobyarchick (1986) derived

Fig. 15. (a) Equal-area projection (Section 4.4) of data points $\mathbf{x}^{(1)}, \ldots, \mathbf{x}^{(100)}$ on H^2. The points make an elliptical cluster, indicating a pre-strain anisotropic fabric. Cross and white polygon indicate the optimal strain and its 95% confidence region. The parameters ζ (Eq. (17)) and ψ are the polar coordinates of the equal-area projection. (b) Close-up of the confidence region (solid line). The optimal solution and its confidence region were determined upon H^2, and visualized on this Euclidean plane. The 95% confidence region determined not by the Mahalanobis but by the hyperbolic distances is shown by dotted line.

Fig. 16. Confidence region (thick line) on H^2 determined as the envelope containing the specified fraction of bootstrap solutions (dots) near the optimal solution (cross).

a formula for describing the attractor of the major-axis orientations of the particles as a function of the aspect ratio of a particle and W_m, the mean kinematic vorticity number of the flow field. According to Passchier (1987, p. 685), the function is rewritten as

$$\psi = \sin^{-1}\left[\frac{W_m}{\tanh \rho}\left(\sqrt{1 - W_m^2} - \sqrt{\tanh^2\rho - W_m^2}\right)\right] \qquad (24)$$

where ρ and ψ are hyperbolic spherical coordinates. The angle ψ is measured from the shearing direction. Circular particles rotate in the rotation sense concordant with the vorticity of the flow, but long particles can rotate backward. The line denoted by Eq. (24) is the separatrix, meaning that the line separates H^2 into two regions. That is, particles represented by points on the different sides of the line rotate in different senses. So, Simpson and De Paor (1993, 1997) proposed the porphyroclast hyperbolic distribution method, which uses the rotation senses in conjunction with ρ and ψ values of particles to determine the position of the separatrix and further to constrain a W_m value. Simpson and De Paor showed that a hyperbola enclosing all points representing back-rotated particles indicates this line on their hyperbolic net (De Paor, 1988). A limb of the hyperbola is asymptote to the shearing direction.

The method of Simpson and De Paor (1993, 1997) is simplified by means of the gnomonic net, where the entire surface of H^2 is mapped onto the disk with the unit radius (Fig. 12), whereby W_m value is obtained by simple graphical procedures. On this net, the separatrix is a chord, an end of which exists at the point of infinity with the parameters $\rho = \infty$ and $\psi = 0$. The other end indicates the W_m value (Fig. 17). The W_m value is determined by finding a straight line on the net to separate points of back-rotated particles from other points (Appendix A).

Fig. 17 shows an example of the graphical method applied to artificial data. This is a difficult example in that the cluster of points corresponding to back-rotated particles partly overlaps that of other particles. Dashed lines in this figure are chords meeting at the point of infinity parallel to the foliation, and show the possible range of the separatrix. That is, if the line through the data point with the label 'a' is chosen, the upper-right side of the line includes not only the data with backward rotations but also four data points with forward rotations. If the other line is chosen, the lower-left side of the line includes all the data points with forward rotations and those with backward rotations as well. There is no line for the clear separation of rotation senses.

This problem is a special case of linear discriminant analysis, which seeks a line to separate data points on a plane according to the labels linked to the data (Duda et al., 2001). In the case of Fig. 17a, the separator is a ray from the point indicated by the triangle in the figure, and the labels are the rotation senses.

Here, we evaluate the goodness of position of the borderline to determine the optimal value and uncertainty of W_m. Points corresponding to back-rotated particles should be plotted on the upper-right side of the borderline, but the points are plotted on the both sides of a borderline in this range. Let n_B be the number of those points on the lower-left side of a borderline, and n_F be the number of points corresponding to forward-rotated particles on the upper-right side of the line. The total number of data is n. Accordingly,

$$ER = \max(n_B, n_F)/n \qquad (25)$$

is the error rate of the position of the borderline. Namely, the optimal value of W_m is determined by positioning the separatrix to minimizing this rate.

In order for counting the numbers n_F and n_B, we need a simple criteria to judge which side of the separating line a data point exists on the gnomonic map. To understand the criteria, suppose the point P in Fig. 18. The W_m value corresponding to the line AP is obtained from the polar coordinates, ζ and ψ, of P as follows. Since the right

triangles ABC and CBE in Fig. 18 are similar to each other, the line AP is expressed in terms of the Cartesian coordinates A-pq as $q = p \tan(\pi/2 - \theta_0)$. This tangent equals the ratio of the lengths FP abd AF, which further equal $\zeta \sin \psi$ and $(1 - \zeta \cos \psi)$, respectively. It follows that

$$\tan\left(90^\circ - \theta_0\right) = \zeta \sin\psi/(1 - \zeta\cos\psi). \qquad (26)$$

It follows from Eqs. (26) and (A.4) that

$$W_m = \mathrm{RHS}/\sqrt{\mathrm{RHS}^2 + 1}, \qquad (27)$$

where RHS is the right-hand side of Eq. (26).

In the case of Fig. 17, the range $W_m = 0.493$–0.583 indicates the maximum possible uncertainty. The ER value is minimized in the interval $W_m = 0.535$–0.556, the midpoint of which gives the optimal W_m value at 0.546. In case where the clusters of different rotation senses are clearly separated on the gnomonic projection, there is the interval of W_m where $n_B = n_F = 0$ (Fig. 19). The interval marks the uncertainty of W_m value for the given data set, and the optimal W_m value is obtained as the midpoint of the interval.

6. Comparison with previous methods

6.1. Techniques for determining coaxial strain

6.1.1. Method of Mulchrone et al. (2003)

The method of Mulchrone et al. (2003) for determining optimal strain from R_f/ϕ data is equivalent to the present one, though formulations are different. The methods have different techniques for error estimation.

First, Mulchrone et al. (2003) normalize an ellipse by its area being equal to π. Then, they express an ellipse using its moving radius $\ell(\varphi)$ (Fig. 1). Their basic idea is that the mean of moving radii of post-strain ellipses may approximate the strain ellipse, if the ellipses have the centers at the same point (Fig. 20). To this end, they introduce the expression

$$1/\ell^2 = p - (m\cos\psi)\cos 2\varphi - (m\sin\psi)\sin 2\varphi \qquad (28)$$

for an ellipse with the major-axis orientation $\phi/2$, where the parameters $p = R/2 + 1/2R$ and $m = R/2 - 1/2R$ characterize the ellipse shape (Mulchrone et al. 2003, Eq. 10). Using Eqs. (7) and (8), we obtain $p = \cosh\rho = x_0$ and $m = \sinh\rho = r$, where r and x_0 are the cylindrical coordinates of a point $\mathbf{x} = (p, m\cos\psi, m\sin\psi)^T$ on H^2 (Fig. 4). It follows from Eq. (28) that

$$1/\ell^2 = -\mathbf{x} \circ \boldsymbol{\chi}, \qquad (29)$$

where $\boldsymbol{\chi} = (1, \cos 2\varphi, \sin 2\varphi)^T$ indicates a point on ∂D in Fig. 4. The right-hand side of Eq. (29) is guaranteed to be positive in sign, because both $\mathbf{x}$ and $\boldsymbol{\chi}$ have the end points above and on the cone (Section 4.1).

Suppose that we have n ellipses. We take the generalized mean with the power -2 of the moving radii of the n ellipses ℓ_s such that
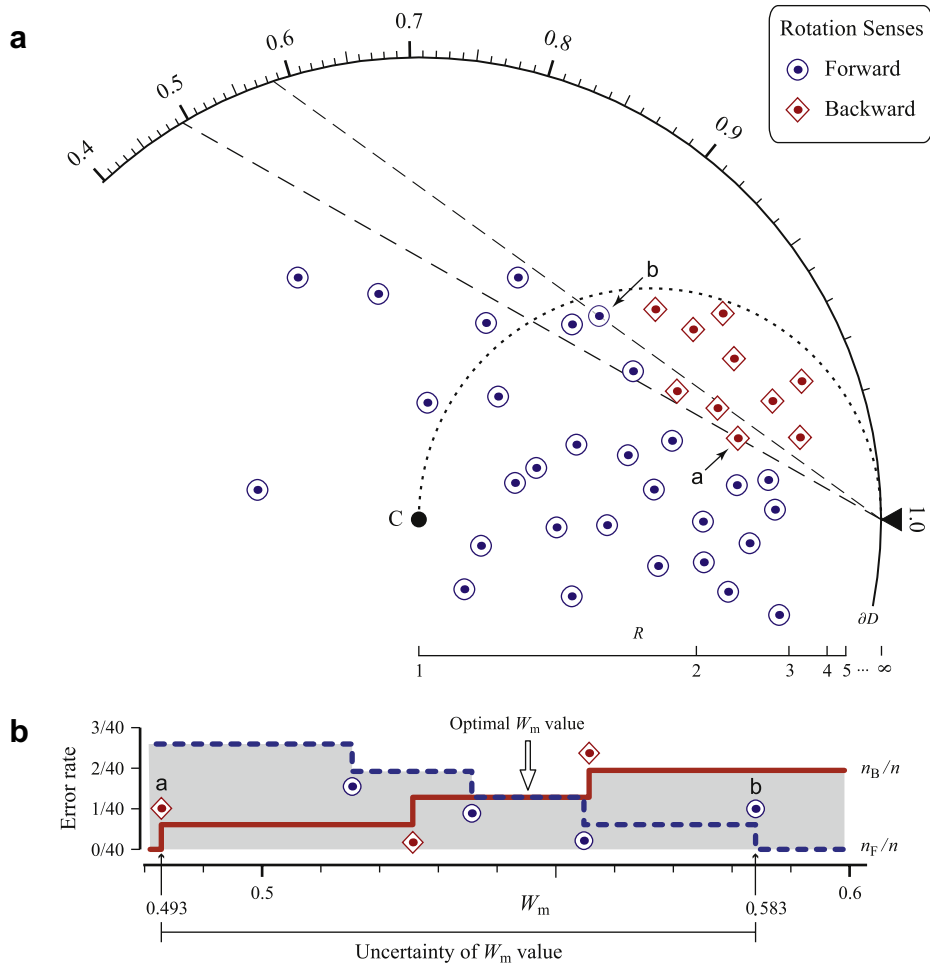
$$(\ell_s)^{-2} \equiv \frac{1}{n}\left\{\left[\ell^{(1)}\right]^{-2} + \cdots + \left[\ell^{(n)}\right]^{-2}\right\}, \qquad (30)$$

where $\ell^{(i)}$ is the ith radius. Combining Eqs. (29) and (30), we have

$$(\ell_s)^{-2} = \frac{1}{n}[-\mathbf{x}_f^{(1)} \circ \boldsymbol{\chi} - \cdots - \mathbf{x}_f^{(n)} \circ \boldsymbol{\chi}] = -\frac{1}{n}[\mathbf{x}_f^{(1)} + \cdots + \mathbf{x}_f^{(n)}] \circ \boldsymbol{\chi}$$

Rearranging this equation, we obtain

$$\left(\sqrt{\|\boldsymbol{\lambda}\|/n}\,\ell_s\right)^{-2} = -\widehat{\mathbf{x}}_s \circ \boldsymbol{\chi}, \qquad (31)$$

a

b

Fig. 17. (a) Schematic illustration showing the determination of the mean kinematic vorticity number W_m on the gnomonic net for the data that consist of the shapes, orientations and rotation senses of 40 rigid particles. Solid lines through the points with the labels 'a' and 'b' indicate the possible range of the line separating rotation senses. The upper-left ends of the lines indicate the lower and upper limits of the number for this artificial data set. Dotted line from solid circle to triangle indicates the horocycle on H^2 denoted by Eq. (A2). (b) The optimal W_m value for the data determined as the midpoint of the interval of minimum error rate (Eq. (25)).

where $\hat{\mathbf{x}}_s$ is the hyperbolic vector mean in Eq. (20) and λ is the resultant vector (Eq. (21)). Comparison of Eqs. (29) and (31) leads us to the interpretation that $\sqrt{\|\lambda\|/n}\,\ell_s$ is the moving radius of the strain ellipse that is represented by $\hat{\mathbf{x}}_s$. Jensen (1981, p. 200) shows

$\|\lambda\| \ge n$, where equality holds only if all the n ellipses are identical. Therefore, ℓ_s denotes the moving radius of an ellipse similar to and smaller than the strain ellipse (Fig. 20). The explanation on ℓ_s by Mulchrone et al. (2003) is misleading, because they suggest as if ℓ_s is the arithmetic mean of the moving radii (especially their Fig. 2).

It is obvious in our formulation that the limitations made by Mulchrone et al. (2003, p. 530) are not essential. They limited the applicability of their method to such cases where (1) ψ_i is a uniform random variable on the $[0, 2\pi]$ interval, and (2) the variable R_i is independent from ϕ_i. That is, distribution of the points $\mathbf{x}_i^{(1)}, ..., \mathbf{x}_i^{(n)}$
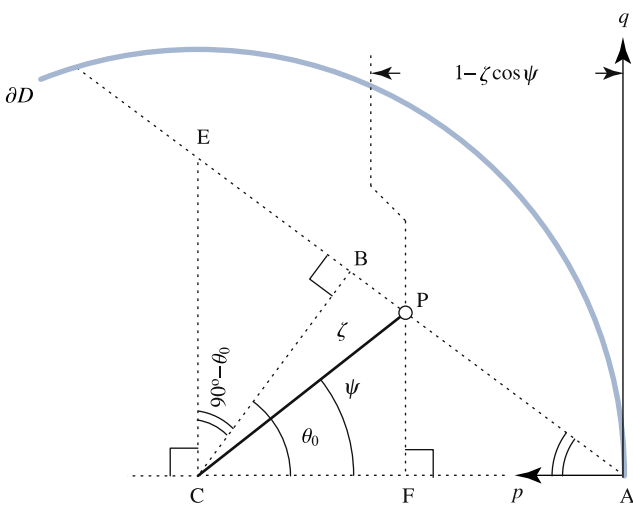
Fig. 18. Schematic illustration for deriving Eq. (26).
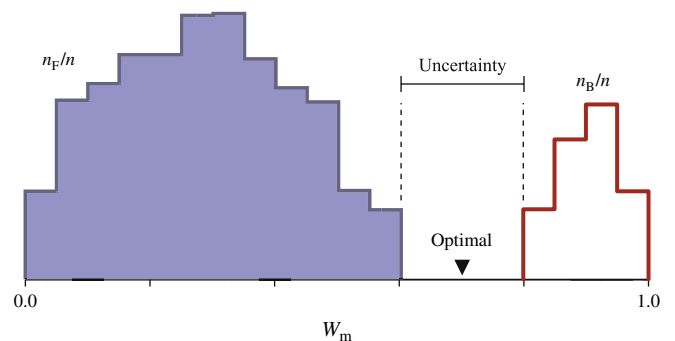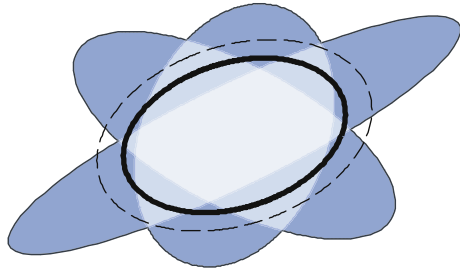

Fig. 19. Optimal value and uncertainty of W_m.

Fig. 20. Three ellipses illustrating three R_f/φ data. Dashed and thick lines indicate the strain ellipse determined as the hyperbolic vector mean $\hat{\mathbf{x}}_s$ and ℓ_s determined by Eq. (31) for the data.

is assumed to have rotational symmetry with respect to the point C. Their optimal strain is identical with that indicated by our hyperbolic vector mean. The necessary condition of the latter is that the centroid of the points $\mathbf{x}_i^{(1)}, ..., \mathbf{x}_i^{(n)}$ is located at the point C. This is looser than the two conditions. For example, the data in Fig. 14 satisfy neither of their conditions. That is, those points are distributed along an elliptical line on the equal-area projection, but we have obtained the accurate solution via the hyperbolic vector mean.

Mulchrone et al. (2003) estimate the confidence intervals of R_s and ϕ_s by means of the bootstrap resampling, and the cluster size of bootstrap solutions on the conventional $\log R - \phi$ plot (Fig. 3) is used to evaluate the intervals. Accordingly, their estimate is largely identical with ours (Fig. 16), when the cluster does not include the point C on H^2 like the region A in Fig. 21. If a confidence region on H^2 include this point like the region B in this figure, the intervals cannot be evaluated.

In contrast, our error estimation firstly draws a closed loop on H^2 for denoting a confidence region. So, a confidence region is clearly defined for the both cases in Fig. 21. Then, the confidence intervals of R_s and ϕ_s are evaluated from the loop, but this second step is not done for the case B. Definition of appropriate distance in a parameter space is essential to define such a confidence region whatever the parameter space is. The hyperboloid model meets this demand.

6.1.2. Method of Yamaji (2005)

The method of Yamaji (2005) calculates an optimal strain ellipse and its error from R_f/ϕ data. It can deal with data with pre-strain anisotropy, but has a weakness. That is, optimal solutions become inaccurate when the spread of data is large (Yamaji, 2005, Figs. 9 and 10), though the inaccuracy is practically small. The reason for this is now understood. The present method has no such inaccuracy.

Yamaji (2005) assumed that the pre-strain points obey a bivariate normal distribution (Johnson and Wichern, 2003) with the mean at the origin of the equidistant projection, which has the polar coordinates ρ and ψ. Let us use the bold capital letter $\mathbf{X}$ to represent a point and the corresponding position vector on this projection. Once a point on the projection $\mathbf{X}_s = (\rho_s \cos\psi_s, \rho_s \sin\psi_s)^T$ is assumed to represent strain, the pre-strain points $\mathbf{X}_i^{(1)}, ..., \mathbf{X}_i^{(n)}$ are easily obtained from the post-strain points $\mathbf{X}_f^{(1)}, ..., \mathbf{X}_f^{(n)}$ using Eqs. (1) and (2). So, the method of Yamaji (2005) seeks out the point $\mathbf{X}_s$, thereby the likelihood of the bivariate normality applies best to the pre-strain points. The unlikeness is evaluated by Hotelling's T^2 statistic (Johnson and Wichern, 2002),

$$T^2 = [\mathbf{X}_i^{(1)}]^T \mathbf{S} \mathbf{X}_i^{(1)} + \cdots + [\mathbf{X}_i^{(n)}]^T \mathbf{S} \mathbf{X}_i^{(n)}$$

where

$$\mathbf{S} = \frac{1}{n-1} \{ [\mathbf{X}_i^{(1)}]^T \mathbf{X}_i^{(1)} + \cdots + [\mathbf{X}_i^{(n)}]^T \mathbf{X}_i^{(n)} \}$$
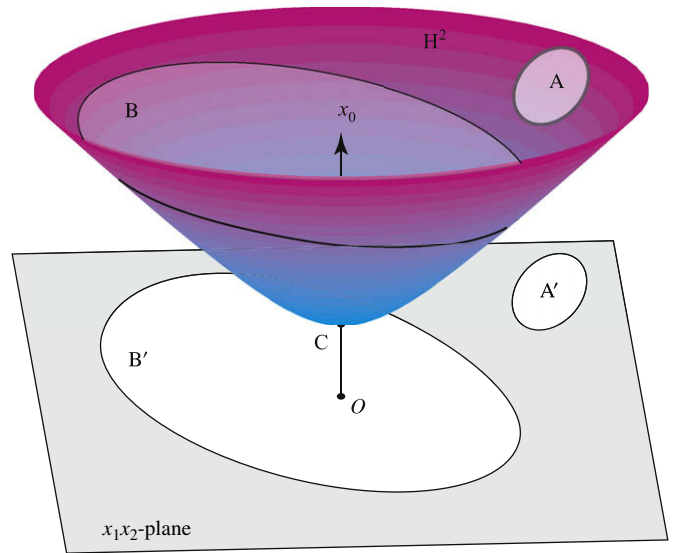

Fig. 21. Confidence regions A and B on H^2, the latter of which includes the point C. A′ and B′ are the orthogonal projections of the regions onto the $x_1 x_2$-plane.

is the covariance matrix of the pre-strain points about the origin. $\mathbf{S}$ and T^2 are functions of the data $\mathbf{X}_f^{(1)}, ..., \mathbf{X}_f^{(n)}$ and of the strain to be determined. Accordingly, the optimal strain for a given data set is obtained by seeking out the strain that minimizes T^2.

This method gradually becomes inaccurate with the increasing spread of those vectors. Two factors affect this accuracy. Distortion of the equidistant projection increases with the distance from the point C on H^2. Accordingly, if the cluster of the pre-strain points is large, this effect becomes significant. To avoid the distortion, a hyperboloid distribution (Barndorff-Nielsen, 1987; Jensen, 1981) should be utilized instead of the bivariate normal distribution. More important factor is statistical. Maximum likelihood estimation is a popular statistical method used to calculate the best way of fitting a mathematical model for some data (Van den Bos, 2007). The estimation has optimal properties for statistical parameter estimation. For example, the estimated parameters asymptotically approaches the true ones with increasing number of data. The minimization of T^2 has no such properties. The maximum likelihood estimate of strain with the assumption above is obtained by maximizing

$$L = -\frac{n}{2}T^2 - \frac{n}{2}\log|\mathbf{S}| - n\log 2\pi. \tag{32}$$

This is called the likelihood function, and is derived in Appendix C. Since $\mathbf{S}$ indicates dispersion of the pre-strain points, the effect of the second term in the right-hand side of this equation become significant relative to the first term with the increase of this spread. This leads to the inaccuracy of Yamaji (2005) method.

The fact is that the hyperbolic vector mean (Eq. (20)) is the maximum likelihood estimate of the mean of a hyperboloid distribution (Jensen, 1981). Random work from a point on a Euclidean plane results in a density distribution obeying a bivariate normal distribution, whereas that on a unit sphere obeys a von Mises–Fisher distribution (e.g., Mardia and Jupp, 1999). The distribution on H^2 is known to obey a hyperboloid distribution (Jensen, 1981). Accordingly, the strain ellipse represented by the mean is the most appropriate estimate if we have no *a priori* information on data or strain. Arithmetic mean and standard deviation are useful in many cases when the vectors are in a Euclidean space, even if the statistical distribution of the vector population is uncertain. The variation of shapes and orientations of deformed fossil part such as those in Fig. 14 does not obey a hyperboloid distribution. However, the

hyperbolic vector mean gives accurate strain ellipse in both cases. This is because coaxial strain is represented by a rigid-body movement of the cluster of points on H^2, and the centroid of the initial cluster is mapped to the centroid of the final one. Therefore, the present method determines perfectly accurate strain, provided that the initial centroid was at the point C on H^2.

6.1.3. Theta-curve method

The θ-curve method of Lisle (1977) is the fist computerized technique for determining strain from R_f/ϕ data, and utilizes a mathematical inversion with the assumption that the pre-strain orientations $\phi_i^{(1)}, \ldots, \phi_i^{(n)}$ obey a uniform distribution. Namely, the optimal strain is determined so as to maximize the χ^2 statistic that is the function of R_s and ϕ_s indicating the uniformity of the orientations.

This inverse method has weakness. First, pre-strain grain fabric is assumed to be isotropic, but sedimentologists have described anisotropic fabrics possibly suggesting sedimentary environments (Potter and Pettijohn, 1963; Griffiths, 1967; Middleton and Southerd, 1977). Second, this method is known to be numerically unstable, thereby error estimation based on the method is difficult (Yamaji, 2005). Specifically, χ^2 has multiple peaks for a dataset. As a result, the uncertainly of the optimal strain for the data is denoted not by a simply connected confidence region but by multiple confidence regions on the $R_s - \phi_s$ plot. In order to stabilize the mathematical inversion to estimate strain, not only the initial orientations but also initial aspect ratios of strain markers should be taken into account (Yamaji, 2005). The methods of Mulchrone et al. (2003) and Yamaji (2005) and of the present article have no such instability.

6.2. Kinematic vorticity analysis

There are a few techniques to estimate mean kinematic vorticity number W_m. Those of Passchier (1987) and Wallis (1992) utilize the critical aspect ratio R_c below which rigid particles continuously rotate and hence their long-axis orientations have a large variation, and above which they display a preferred orientation. R_c has a one-to-one correspondence with W_m. Finding this threshold from shape fabric is feasible, but R_c value is often ambiguous. Many samples show a gradual decrease in the variation of long-axis orientations. As a result, the interval in which the variation exhibits a rapid drop is used as the uncertainty (e.g., Law et al., 2004). Depending on tectonic settings, the gradual change may have several origins, including initial preferred orientations prior to the onset of deformation, heterogeneous flow field owing to the interaction between particles or to the heterogeneous rheology of the matrix.

Statistically relevant error estimation is not easy for the technique of finding R_c because of the difficulty of statistical modeling of shape fabric below the threshold. It is inappropriate to assume a uniform distribution for long-axis orientations, because rotation velocity depends on the orientation. Although particles fatter than this threshold rotate continuously, their angular velocities depend on long-axis orientations (Jeffrey, 1922). As a result, the orientations have tendency to have a preferred orientation around which the rotations are retarded.

The hyperbolic distribution method by Simpson and De Paor (1997) and its variants including the techniques using the gnomonic net (Section 5.2) utilize not only R_c but also the decreasing pattern to estimate W_m. The advantage of the technique using the gnomonic net is that both an optimal W_m value and its uncertainty are estimated graphically only with a ruler and the net in Fig. 12.

The uncertain statistical distribution of long-axis orientations hinders the quantitative estimation of the specific percentile interval of W_m, e.g., a 95% confidence interval. Owing to this difficulty, we estimate the uncertainty by the interval of mis-classification in Fig. 17b or by the gap.

By means of the simplified hyperbolic distribution method, Forte and Bailey (2007) applied bootstrap method only to back-rotated particles for evaluating the confidence interval of W_m. Namely, they dealt only with those particles, and the maximum ψ value of the particles was assumed to be equal with θ_0 in Figs. 18 and A1. Then, the W_m value corresponding to the maximum was calculated through Eq. (A.4). Bootstrap samples were taken only from those particles, and the maximum was determined for each of the samples to calculate W_m. The maximum ψ value of the samples was assumed to be equal to that of the population which is represented by the samples. It follows that the true population maximum was smaller than the observed maximum. The particles with large ψ values are thought of as 'outliers,' meaning that increasing number of back-rotated particles was expected to clarify those being exceptional. However, the assumption does not always hold. Instead, it is improbable that there is a generally relevant statistical distribution for the shape fabric of porphyroclasts. It is equally possible that the statistical distribution of ψ of back-rotated particles have a heavy tail, in which samples have large ψ values. Their error analysis is not appropriate in this case.

Acknowledgments

Appendix A. Gnomonic projection and vorticity analysis

The line defined by Eq. (24) is demonstrated in this appendix to be a geodesic on H^2 using the gnomonic projection. In this case, the geodesic lies on a plane the x_0-axis. In terms of the polar coordinates (ζ, θ) on the gnomonic projection (Section 4.4.2), Eq. (24) is simplified to

$$\zeta \sin\theta = W_m\left(\sqrt{1 - W_m^2} - \sqrt{\zeta^2 - W_m^2}\right), \tag{A.1}$$

where the relationship between ζ and R is given by Eq. (18), and $\theta = \psi = 2\phi$ is assumed for the projection. Points at infinity from the point C on H^2 have the radial coordinate $\zeta = 1$. The polar coordinates constrained by Eq. (A.1) indicate a line on the gnomonic projection. This line is referred to as L.

The points A and B in Fig. A1 are the ends of L. First, we show that the triangle ABC has a right angle at B. The point A is defined by $\zeta = 1$, and represents the infinitely long ellipse, $R = \infty$ and $\phi = 0$. The length AC equals 1, because points at infinity from C on H^2 are mapped onto the unit circle. The end B of L is defined by $\zeta = W_m$, because $\sqrt{\zeta^2 - W_m^2}$ in Eq. (A.1) is imaginary for $\zeta < W_m$. This reflects the fact that circular particles in the physical space cannot rotate backward. At the point B, Eq. (A.1) reduces to

$$\sin\theta_0 = \sqrt{1 - W_m^2}. \tag{A.2}$$

The lengths of AC and BC are 1 and W_m, respectively. It follows from Eq. (A.2) that ABC is a right triangle with the side AC being the hypotenuse and $\angle$ABC $= 90°$. The circle with the diameter AC circumscribes this triangle and inscribes ∂D. Such a circle on the gnomonic projection is a horocycle through the point C on H^2.

In order to show that the point P(ζ, θ) satisfying Eq. (A.1) is constrained on the straight line AB, we assume that P can deviate fro this line. The distance of P from AB is referred to as s. It is obvious from Fig. A1 that $\overline{PU} = \zeta \sin\theta$, which is rewritten by Eq. (A.1) as
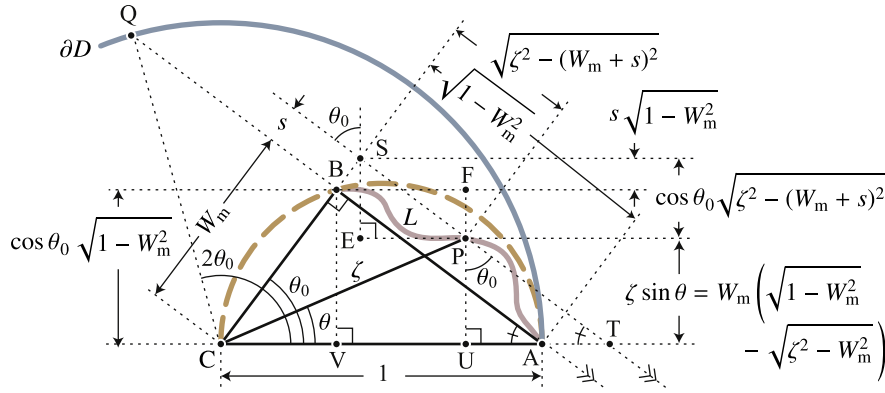
Fig. A1. Gnomonic projection of H^2 for the explanation of vorticity analysis. Thick curve L is the line denoted by Eq. (A1). A and B are the ends of the curve. ∂D is the circle shown in Fig. 4, and represent points at infinity from C on H^2. P indicates the point with the polar coordinates (ζ, θ), which satisfy Eq. (A1). Dashed line is the semicircle that circumscribes $\triangle$ABC and inscribes ∂D. Line ST through P is parallel to the side AB. Lines PU and BV are perpendicular to AC.

$$\overline{PU} = W_m \left(\sqrt{1 - W_m^2} - \sqrt{\zeta^2 - W_m^2} \right). \tag{A.3}$$

The right triangle ABC has the side $\overline{BC} = \sqrt{1 - W_m^2}$. So, $\overline{BV} = \cos\theta_0 \sqrt{1 - W_m^2}$. The right triangle CPS has the side $\overline{SP} = \sqrt{\zeta^2 - (W_m + s)^2}$, where s is the distance of P from AB. It follows that $\overline{SE} = \cos\theta_0 \sqrt{\zeta^2 - (W_m + s)^2}$. Since W_m has a value in the range from 0 to 1, the formula (Bobyarchick, 1986; Passchier, 1986),

$$\cos\theta_0 = W_m, \tag{A.4}$$

is obtained from Eq. (A.2). Accordingly, we have $\overline{BV} = W_m \sqrt{1 - W_m^2}$. Substituting this in to Eq. (A.3), we obtain $\overline{PU} = \overline{BV} - W_m \sqrt{\zeta^2 - W_m^2}$ and $\overline{PF} = W_m \sqrt{\zeta^2 - W_m^2}$. It follows that $\overline{SE} = \overline{PF} + s\sqrt{1 - W_m^2}$. Rewriting this, we arrive at the equation,

$$W_m \sqrt{\zeta^2 - (W_m + s)^2} = W_m \sqrt{\zeta^2 - W_m^2} + s\sqrt{1 - W_m^2}.$$

The deviation s should vanish in order for this equation to hold for any ζ greater than W_m. That is, the line L must coincide with the straight line AB in Fig. A1. Straight lines on the gnomonic projection are images of geodesics on H^2. Thus, the line defined by Eq. (24) has been proved to be such a geodesic.

Given a W_m value, the point Q can be uniquely determined. That is, CB is the perpendicular bisector of the chord AQ. So, $\angle$ACQ $= 2\theta_0$. From Eq. (A.4), we obtain the equation (Bobyarchick, 1986)

$$2\theta_0 = 2\cos^{-1}W_m \tag{A.5}$$

Appendix B. Relationship between pole vector and mean kinematic vorticity number

The separating line AQ in Fig. A1 is a straight line on the gnomonic projection, meaning that it is a shadow of a geodesic on H^2. The pole vector $\mathbf{v}$ of this geodesic is determined as follows. The point B in this figure indicates the point on the geodesic nearest from the point C on H^2. From Fig. A1 and Eq. (18), we have $\overline{CB} = W_m = \tanh\varrho$, where $\overline{CB}$ and ϱ are the lengths of CB on the projection and on H^2, respectively. It follows that the point corresponding to B on H^2 has the Cartesian coordinates $(\cosh\varrho, \sinh\varrho \cos\theta_0, \sinh\varrho \sin\theta_0)$. The position vector with those

components is perpendicular to the pole vector $\mathbf{v}$, which exists on the plane containing the point and the x_0-axis. Therefore, we obtain $\mathbf{v} = (\sinh\varrho, \cosh\varrho \cos(\theta_0 + \pi), \cosh\varrho \sin(\theta_0 + \pi))^T$. Then, inclination of this vector is $v_0/v_r = \sinh\varrho/\cosh\varrho = \tanh\varrho = W_m$, where v_0 and v_r are the cylindrical components of the pole vector.

Appendix C. Maximum likelihood estimation of bivariate normal distribution

Eq. (32) is derived as follows. The pre-strain vectors were assumed to obey the bivariate normal distribution with the probability density

$$p(\mathbf{X}_i) = \frac{1}{2\pi|\mathbf{S}|^{1/2}}\exp\left(-\frac{1}{2}\mathbf{X}_i^T\mathbf{S}\mathbf{X}_i \right).$$

If data are statistically independent from each other, the probability of obtaining a specific set of R_f/φ data equals the product, $p(\mathbf{X}_i^{(1)})\cdots p(\mathbf{X}_i^{(n)})$. Consequently, the optimal strain ellipse is determined by maximizing this probability or equivalently the logarithm of the probability. Eq. (32) denotes this logarithm. The optimal strain is the most likely estimate for given R_f/φ data.

References

Aitchison, J., 1986. The Statistical Analysis of Compositional Data. Chapman and Hall, London.

Barndorff-Nielsen, O., 1987. Differential and Integral Geometry in Statistical Inference. In: Gupta, S.S. (Ed.), Differential Geometry in Statistical Inference. Institute of Mathematical Statistics, Hayward, pp. 95–161.

Brace, W.F., 1961. Mohr construction in the analysis of large geologic strain. Bulletin of Geological Society of America 72, 1059–1080.

Bobyarchick, A.R., 1986. The eigenvalues of steady flow in Mohr space. Tectonophysics 122, 35–51.

Chadwick, P. 1999. Continuum Mechanics: Concise Theory and Problems, second Expanded Ed. Dover, Mineola.

Cloos, E., 1947. Oolite deformation in the South Mountain Fold, Maryland. Bulletin of Geological Society of America 58, 843–918.

Davison, A.C., Hinkley, D., 1997. Bootstrap Methods and Their Application. Cambridge University Press, Cambridge.

De Paor, D.G., 1983. Orthographic analysis of geological structures – I. Deformation theory. Journal of Structural Geology 5, 255–277.

De Paor, D.G., 1988. R_f/φ_f strain analysis using an orientation net. Journal of Structural Geology 10, 232–333.

De Paor, D.G., 1993. Strain and kinematic analysis in general shear zones. Journal of Structural Geology 15, 1–20.

Duda, R.O., Hart, P.E., Stork, D.G., 2001. Pattern Classification, second ed. John Wiley and Sons, New York.

Dunnet, D., 1969. A technique of finite strain analysis using elliptical particles. Tectonophysics 7, 117–136.

Egozcue, J.J., Pawlowsky-Glahn, V., Mateu-Figueras, G., Barceló-Vidal, 2003. Isometric logratio transformations for compositional data analysis. Mathematical Geology 35, 279–300.

Elliott, D., 1970. Determination of finite strain and initial shape from deformed elliptical objects. Geological Society of America Bulletin 81, 222–2236.

Faber, R.L., 1983. Foundations of Euclidean and Non-Euclidean Geometry. Dekker, New York.

Flinn, D., 1956. On the deformation of the Funzie Conglomerate, Fetlar, Shetland. Journal of Geology 64, 480–505.

Forte, A.M., Bailey, C.M., 2007. Testing the utility of the porphyroclast hyperbolic distribution method of kinematic vorticity analysis. Journal of Structural Geology 29, 983–1001.

Ghosh, S.K., Ramberg, H., 1976. Reorientation of inclusions by a combination of pure and simple shear. Tectonophysics 34, 1–70.

Griffiths, J.C., 1967. Scientific Method in Analysis of Sediments. McGraw-Hill, New York.

Haughton, S., 1856. On slaty cleavage and the distortion of fossils. Philosophical Magazine, Series 4 12, 1–13.

Hossack, J.R., 1968. Pebble deformation and thrusting in the Bygdin area (southern Norway). Tectonophysics 5, 315–339.

Jeffrey, G.B., 1922. The motion of ellipsoidal particles immersed in a viscous fluid. Proceedings of the Royal Society of London, Series A 103, 58–61.

Jensen, J.L., 1981. On the hyperboloid distribution. Scandinavian Journal of Statistics 8, 193–206.

Jessup, M.J., Law, R.D., Frassi, C., 2007. The Rigid Grain Net (RGN): an alternative method for estimating mean kinematic vorticity number (W_m). Journal of Structural Geology 29, 411–421.

Johnson, R.A., Wichern, D.W., 2002. Applied Multivariate Statistical Analysis, fifth ed. Prentice-Hall, Upper Saddle River.

Law, R.D., Searle, M.P., Simpson, R.I., 2004. Strain, deformation temperatures and vorticity of flow at the top of the Greater Himalayan Slab, Everest Massif, Tibet. Journal of Geological Society, London 161, 305–320.

Lisle, R.J., 1977. Clastic grain shape and orientation in relation to cleavage from the Aberystwyth Grits, Wales. Tectonophysics 39, 381–395.

Lisle, R.J., 1985. Geological Strain Analysis: A Manual for the R_f/φ Method. Pergamon Press, Oxford.

Michael, A.J., 1987. Use of focal mechanisms to determine stress: a control study. Journal of Geophysical Research 92, 357–368.

Mardia, K.V., 1972. Statistics of Directional Data. Academic Press, London.

Mardia, K.V., Jupp, P.E., 1999. Directional Statistics. Wiley, Chichester.

Means, W.D., Lister, G.S., Williams, P.F., 1980. Vorticity and non-coaxiality in progressive deformations. Journal of Structural Geology 2, 371–378.

Middleton, G.V., Southerd, J.B., 1977. Mechanics of sediment movement. SEPM Short Course 3, 1.1–10.2.

Mulchrone, K.F., O'Sullivan, F., Meer, P.A., 2003. Finite strain estimation using the mean radial length of elliptical objects with bootstrap confidence intervals. Journal of Structural Geology 25, 529–539.

Mulchrone, K.F., Walsh, K., 2006. The motion of a non-rigid ellipse in a general 2D deformation. Journal of Structural Geology 28, 392–407.

Nakaoka, M., 1993. Introduction to Hyperbolic Geometry: Application of Linear Algebra (in Japanese). Saiensu-sha, Tokyo.

Passchier, C.W., 1986. Flow in natural shear zones – the consequences of spinning flow regimes. Earth and Planetary Science Letters 77, 70–80.

Passchier, C.W., 1987. Stable positions of rigid objects in non-coaxial flow – a study in vorticity analysis. Journal of Structural Geology 9, 679–690.

Passchier, C.W., Simpson, C., 1986. Porphyroclast systems as kinematic indicators. Journal of Structural Geology 8, 831–843.

Passchier, C.W., Trouw, R.A.J., 2005. Microtectonics, second ed. Springer, Berlin.

Potter, P.E., Pettijohn, J.F., 1963. Paleocurrents and Basin Analysis. Springer, Berlin.

Ramberg, H., 1975. Particle paths, displacement and progressive strain applicable to rocks. Tectonophysics 28, 1–37.

Ramsay, J.G., 1967. Folding and Fracturing of Rocks. McGraw-Hill, New York.

Ramsay, J.G., Huber, M.I., 1983. The Techniques of Modern Structural Geology. In: Strain Analysis, vol. 1. Academic Press, London.

Ratcliffe, J.G., 2006. Foundations of Hyperbolic Manifolds, second ed. Springer, New York.

Reynolds, W.F., 1993. Hyperbolic geometry on a hyperboloid. American Mathematical Monthly 100, 442–455.

Sato, K., Yamaji, A., 2006. Embedding stress difference in parameter space for stress tensor inversion. Journal of Structural Geology 28, 957–971.

Simpson, C., De Paor, D.G., 1993. Strain and kinematic analysis in general shear zones. Journal of Structural Geology 15, 1–20.

Simpson, C., De Paor, D.G., 1997. Practical Analysis of General Shear Zones Using Porphyroclast Hyperbolic Distribution Method: An Example from the Scandinavian Caledonides. In: Sengupta, S. (Ed.), Evolution of Geological Structures in Micro- to Macro-scales. Chapman and Hall, London, pp. 169–184.

Small, C.G., 1996. The Statistical Theory of Shape. Springer, New York.

Truesdell, C., 1954. The Kinematics of Vorticity. Indiana University Press, Bloomington.

Van den Bos, A., 2007. Parameter Estimation for Scientists and Engineers. Wiley, Hoboken, pp. 273.

Vilenkin, N.J., 1968. Special Functions and the Theory of Group Representation. In: Translations of Mathematical Monographs 22. American Mathematical Society.

Wallis, S.R., 1992. Vorticity analysis in a metachert from the Sanbagawa Belt, SW Japan. Journal of Structural Geology 14, 271–280.

Wallis, S.R., 1995. Vorticity analysis and recognition of ductile extension in the Sanbagawa Belt, SW Japan. Journal of Structural Geology 17, 1077–1093.

Wallis, S.R., Platt, J.P., Knott, S.D., 1993. Recognition of syn-convergence extension in accretionary wedges: examples from the Calabrian Arc and the Eastern Alps. American Journal of Science 293, 463–495.

Wellman, H.G., 1962. A graphical method for analysing fossil distortion caused by tectonic deformation. Geological Magazine 99, 348–352.

Wheeler, J., 1984. A new plot to display the strain of elliptical markers. Journal of Structural Geology 6, 417–423.

Yamaji, A., 2005. Finite tectonic strain and its error, as estimated from elliptical objects with a class of initial preferred orientations. Journal of Structural Geology 27, 2030–2042.

Yamaji, A., Masuda, F., 2005. Improvements in graphical representation of fabric data, showing the influence of aspect ratios of grains on their orientations. Journal of Sedimentary Resarch 75, 517–522.

Yamaji, A., Sato, K., 2006. Distances for the solutions of stress tensor inversion in relation to misfit angles that accompany the solutions. Geophysical Journal International 167, 913–942.